VILNIUS UNIVERSITY
CENTER FOR PHYSICAL SCIENCE AND TECHNOLOGY

Dmitriy Shevchenko

INVESTIGATION OF DEFECT-RELATED LUMINESCENCE OF ISOELECTRONICALY DOPED ZINC SELENIDE-BASED SCINTILLATORS

Summary of doctoral thesis
Physical Sciences, Physics (02 P)

Vilnius, 2015

The research work has been carried out in 2010-2014 in the Semiconductor Physics Department and the Institute of Applied Research, Vilnius University.

Scientific supervisor:

Prof. habil. dr. Gintautas Tamulaitis (Vilnius University, Physical Sciences, Physics 02 P)

Defense Council of the Doctoral Thesis in Physical Sciences at Vilnius University:

Chairman:

Prof. habil. dr. Juozas Vidmantis Vaitkus (Vilnius University, Physical Sciences, Physics 02P)

Members:

Dr. Michael Korjik (Belorussian State University, Physical Sciences, Physics 02P),

Prof. dr. Šarūnas Meškinis (Kaunas Technology University, Technology Science, Materials Engineering 08T)

Prof. dr. Vincas Tamošiūnas (Vilnius University, Physical Sciences, Physics 02P)

Prof. habil. dr. Sigitas Tamulevičius (Kaunas Technology University, Technology Science, Materials Engineering 08T)

The official defense of the doctoral thesis will be held in the public session of the Vilnius University Defense Council in Physical Sciences at 10 h on September 25, 2015, in room A119 of the VU Library Scholarly Communication and Information Center, Saulėtekio Ave. 5-III, LT-10222 Vilnius, Lithuania.

The summary of the doctoral thesis has been distributed on August 25, 2015.

The doctoral thesis is available at the Vilnius University Library and at the library of the Center for Physical Sciences and Technology.

VILNIAUS UNIVERSITETAS
FIZINIŲ IR TECHNOLOGIJOS MOKSLŲ CENTRAS

Dmitrij Ševčenko

IZOVALENTIŠKAI LEGIRUOTŲ CINKO SELENIDO SCINTILIACINIŲ KRISTALŲ PRIEMAIŠINĖS LIUMINESCENCIJOS TYRIMAI

Daktaro disertacijos santrauka
Fiziniai mokslai, fizika (02 P)

Vilnius, 2015

Disertacija parengta Vilniaus universiteto Fizikos fakulteto Puslaidininkių fizikos katedroje ir Taikomųjų mokslų institute 2010–2014 metais.

Mokslinis vadovas – prof. habil. dr. Gintautas Tamulaitis (Vilniaus universitetas, fiziniai mokslai, fizika – 02P).

Disertacija ginama Vilniaus universiteto Fizikos mokslų krypties taryboje:

Pirmininkas – prof. habil. dr. Juozas Vidmantis Vaitkus (Vilniaus universitetas, fiziniai mokslai, fizika – 02P)

Nariai:

Dr. Michail Korjik (Baltarusijos valstybinis universitetas, fiziniai mokslai, fizika – 02P)

Prof. dr. Šarūnas Meškinis (Kauno technologijos universitetas, technologijos mokslai, medžiagų inžinerija – 08T)

Prof. dr. Vincas Tamošiūnas (Vilniaus universitetas, fiziniai mokslai, fizika – 02P)

Prof. habil. dr. Sigitas Tamulevičius (Kauno technologijos universitetas, technologijos mokslai, medžiagų inžinerija – 08T)

Disertacija bus ginama viešame gynimo tarybos posėdyje 2015 m. rugsėjo 25 dieną 10.00 valandą VU bibliotekos Mokslinės komunikacijos ir informacijos centre A119 auditorijoje, Saulėtekio al. 5, III rūmai, LT-10222 Vilnius.

Disertacijos santrauka išsiuntinėta 2015 m. rugpjūčio 25 d.

Disertaciją galima peržiūrėti Vilniaus universiteto ir Fizinių ir technologijos mokslų centro bibliotekose ir VU interneto svetainėje adresu: *www.vu.lt/lt/naujienos/ivykiu-kalendorius*

Santrauka

Disertacija yra skirta priemaišinės liuminescencijos izovalentiškai legiruotuose ZnSe scintiliatoriuose tyrimams, kurių pagrindinis tikslas – detaliau suprasti priemaišinės liuminescencijos mechanizmus telūru ir deguonimi legiruotuose ZnSe scintiliaciniuose kristaluose ir susieti šių kristalų liuminescencijos našumą bei laikines charakteristikas su technologiniais auginimo ir terminio apdorojimo parametrais.

Disertacija yra sudaryta iš penkių skyrių. Kiekvieno skyriaus pabaigoje yra pateikiamos apibendrintos išvados.

Pirmajame skyriuje yra pateikiama ZnSe scintiliatorių parametrų ir įvairių priemaišų sąlygotų spindulinės rekombinacijos mechanizmų apžvalga.

Antrajame skyriuje yra pateikiami darbe naudojamų optinės spektroskopijos bei *in situ* protonais žadinamos liuminescencijos tyrimų eksperimentų metodikų ir įrangos aprašymai.

Trečiajame skyriuje yra pristatomi rezultatai, gauti atliekant priemaišinės liuminescencijos spektrų palyginamąją analizę įvairiuose izovalentiškai iškaitintuose ir neiškaitintuose ZnSe monokristaluose. Pateikiami iškaitintų ZnSe(Te), ZnSe(O), ZnSe(O,Al) ir ZnSe kristalų priemaišinės liuminescencijos spektrų temperatūrinės priklausomybės tyrimų rezultatai, gauti liuminescenciją žadinant kristalų paviršiuje bei tūryje, įvertinamos donorų ir akceptorių šiluminės jonizacijos energijos, fononų energijos bei elektron-fononinės sąveikos stiprumas, centrui relaksuojant iš sužadintos į pagrindinę būseną. Aptariami priemaišinės liuminescencijos juostų intensyvumo priklausomybės nuo temperatūros, gesimo kinetikų ir fotoliuminescencijos sužadinimo spektrų skaitinio modeliavimo rezultatai.

Ketvirtajame skyriuje yra aptariami kolegiravimo retųjų žemių oksidais, skirto sumažinti pošvytį ZnSe scintiliatoriuose, tyrimų rezultatai. Pateikiami gesimo kinetikų modeliavimo rezultatai esant stipriajam (matuoti su laikine skyra) ir silpnajam (matuoti su fazine skyra) žadinimui, absoliutinės kvantinės išeigos priklausomybės nuo žadinančiojo fotono energijos tyrimai. Identifikuojamos priežastys, nulemiančios kolegiruotų ZnSe(Te) scintiliatorių našumo sumažėjimą. Įvertinti deguonies ir telūro sąlygotų defektų efektiniai krūviai.

Penktas skyrius yra skirtas protonais švitinamo įprastinio ZnSe(Te) scintiliatoriaus priemaišinės liuminescencijos *in situ* tyrimams. Pateikiami protonais sužadintos liuminescencijos spektrų ir laisvųjų krūvininkų gesimo kinetikų tyrimų rezultatai, esant skirtingiems protonų įtėkiams. Įvertinama radiacinių defektų generavimo sparta, aptariamos rekombinacijos mechanizmų ypatybės krūvininkų poras žadinant protonais bei šviesa.

Disertacijos pabaigoje pateikiamas cituojamos literatūros sąrašas.

Acknowledgement

Firstly, I would like to give my thanks to my scientific supervisor prof. Gintautas Tamulaitis for his versatile help in achieving the goal in getting results and writing the thesis.

I sincerely grateful to prof. Eugenijus Gaubas, prof. Vladimir Gavryushin, dr. Tomas Čeponis, dr. Jūras Mickevičius, Jonas Jurkevičius, Augustas Vaitkevičius for sharing their experience and support on measurement equipment and experimental techniques at Vilnius University. Also I acknowledge foreign collaborators from Kharkov from Institute for Scintillation Materials for sharing the samples and performing part of measurements.

I would like to express my heartfelt thanks to my friends, mom and grandmother for their constant support and care and to my secondary school physics teacher Vladimir Ovchinnikov for their selfless physics lessons.

This work has been partially supported by the Lithuanian State Study Found and the Research Council.

List of abbreviation

HE – High – Energy (~2.1 eV) defect-related luminescence band;
LE – Low – Energy (~1.9 eV) defect-related luminescence band;
LE-phonon – phonon, emitted during recombination process in the LE band;
HE-phonon - phonon, emitted during recombination process in the HE band;
NBE - Near-Band-Edge (photoluminescence band);
DAP –Donor-Acceptor Pair;
CBM – Conduction Band Minimum;
VBM – Valence Band Maximum;
"e-A" – electron – acceptor (recombination from CBM to acceptor level);
FWHM –Full Width at Half Maximum;
PL – Photoluminescence;
PI-L – Proton-Induced Luminescence
PLE – Photoluminescence Excitation
EPI – Electron-Phonon Interaction
XL – X-ray Luminescence;
QY – Absolute Quantum Yield;
MW-PC – Microwave-Probed Photoconductivity;
TRPL –Time-Resolved Photoluminescence;
ZPL – Zero-Phonon Line;
CW –Continuous-Wave;
ZnSe:Zn - ZnSe annealed in Zn vapor;
ZnSe(Te) –ZnSe doped by tellurium (or with other impurities, when indicated accordingly);
ZnSe(Te):Zn – ZnSe doped by tellurium and annealed in Zn vapor.

Introduction

A decade ago, zinc selenide has been investigated as a wide-bandgap semiconductor prospective for application in blue light-emitting diodes (LEDs). However, significant problems related to long-term stability of the ZnSe-based LEDs are remained unresolved, while III-nitride materials took currently the lead in LED industry. However, ZnSe with intentionally enhanced defect-related luminescence exhibit good scintillation parameters: high external light yield, low afterglow level (i.e. weak intensity of the slow component of luminescence decay), high thermal stability and radiation hardness. The parameters of defect-related luminescence in ZnSe might be optimized by doping with different impurities. Doping by isoelectronic impurities from a group VI (tellurium, oxygen, sulfur) and subsequent annealing in Zn vapor enable one to enhance the efficiency of the defect-related luminescence by more than one order of magnitude.

Conventional ZnSe scintillators are doped with tellurium. They exhibit the highest luminescence efficiency. In the recent years, tellurium-doped ZnSe scintillators are successfully employed for manufacturing detectors for multi-energy introscopy systems and for low energy X-ray emission. The multi-energy introscopy technique utilizes different scintillators for material identification by detection of X-ray photons at different energies. Thus, even organic materials with similar effective atomic numbers (sugar vs. drugs, etc.) can be effectively identified. Currently, the multi-energy introscopy systems are used for luggage inspection at airports and the customs control points for cargo inspection.

Tellurium-doped ZnSe scintillator is chosen as detector for low-energy ionizing emission because of its high detection efficiency of soft X-rays emission. Meanwhile, doping of ZnSe by oxygen enables growing scintillating crystals with fast response time (1-5 μs). Though the oxygen-doped ZnSe scintillating crystals are poorly studied, it is expected to apply them in inexpensive computed tomography systems. Zinc selenide scintillating crystals attracted considerable attention in the recent years, however, the mechanisms of the radiative transitions involving deep levels are still not well understood. Thus, a study of fundamental mechanisms of the radiative recombination in isoelectronically-ZnSe crystals with intentionally enhanced defect-related luminescence is important to enhance the performance of modern tomography and introscopy systems.

Main objectives

The theses are aimed at the investigation of defect-related mechanisms in zinc selenide scintillating crystals doped with tellurium and oxygen and to relate the luminescence efficiency and response time characteristics with the crystal growth parameters. Main objectives are:

1. to evaluate the influence of doping by tellurium and oxygen and subsequent annealing in Zn vapor on efficiency of the different components of defect-related luminescence band and to investigate the transients of the defect-related photoluminescence and density of photoexcited nonequilibrium carriers;
2. to compare photoluminescence peculiarities at band-to-band and two-step excitation conditions;
3. to evaluate the phonon energy, electron-phonon interaction strength, and zero-phonon line position for defect-related PL in ZnSe crystals doped with tellurium and oxygen using optical spectroscopy techniques;

4. to simulate the dependence of photoluminescence intensity on temperature in oxygen-doped ZnSe;
5. to simulate PL decay kinetics in ZnSe doped with tellurium and oxygen;
6. to investigate defect-related PL spectra and decay kinetics in ZnSe scintillating crystals co-doped with rare earth oxides by using optical spectroscopy techniques;
7. to evaluate oxygen and rare earths role in ZnSe additionally co-doped with rare earth oxides;
8. to perform *in situ* study of defect-related luminescence and nonequilibrium transients in conventional ZnSe(Te) scintillation crystals irradiated by protons and to estimate a generation rate of the radiation defect;
9. to evaluate the peculiarities of recombination mechanisms at the nonequilibrium carriers excitation with protons and visible light;
10. to evaluate the limit value of proton fluence that causes irreversible destruction of ZnSe(Te) scintillation parameters;

Novelty and significance of the thesis

Recently, ZnSe-based scintillation detectors attract considerable attention for application in multi-energy tomography and introscopy systems. However, the fundamental mechanisms of defect-related emission in ZnSe-based scintillators are little studied and poorly understood. The current study allowed getting a deeper insight into the basic mechanisms of defect-related luminescence in ZnSe scintillation crystals. Important relations between the growth conditions of ZnSe scintillating crystals and their luminescence properties were revealed.

The study demonstrates the peculiarities of radiative recombination mechanism in ZnSe doped with tellurium and oxygen:

- a new carrier recombination model in ZnSe(O,Al) and ZnSe(Te) is proposed and numerical simulation of the PL intensity dependence on temperature is performed; numerical simulation of the PL decay kinetics using donor-acceptor pair recombination model and PLE spectra is performed;
- it is revealed, that the changes of defect-related PL parameters in ZnSe scintillation crystals additionally co-doped with rare earth oxides are related to oxygen rather than to rare earth ions; the factors limiting PL efficiency in the oxygen-doped ZnSe are identified; the decrease in PL efficiency in ZnSe(Te) co-doped with rare earth oxides is explained;
- *in situ* study of PL and nonequilibrium carrier transients during irradiation with 1.6 MeV protons of conventional ZnSe(Te) scintillator is performed for the first time in ZnSe(Te);

The points to be maintained

1. The defect-related luminescence band in ZnSe(O,Al) scintillation crystals is caused by optical transitions involving deep donor and acceptor pairs, as in conventional ZnSe(Te) scintillators. Doping of ZnSe crystals with oxygen by adding aluminum oxide into the melt enables achieving a density of optically-active donor and acceptor pairs, which is by an order of magnitude higher than that in the conventional ZnSe(Te) scintillation crystals.

2. Oxygen has stronger effect on the defect-related PL efficiency and the carrier recombination rate that the rare earth elements in the ZnSe(Te) scintillation crystals grown from the melt with rare earth elements oxides.
3. Co-doping of ZnSe(Te) scintillators with rare earth elements by adding their oxides into the melt enhances the nonradiative recombination rate and increases the fraction of carriers recombining via radiative centers resulting in the less thermally stable high-energy band of the defect-related luminescence. As a result, the afterglow is decreased.
4. The conventional ZnSe(Te) scintillator can be utilized for the detection of nonrelativistic protons (<1.6 MeV) at fluencies below 10^{13} cm^{-2}. The proton fluency above 10^{13} cm^{-2} results in fast and irreversibly reduction of the luminescence efficiency due to a decrease in the nonequilibrium carrier lifetime as well as to the irradiation-caused destruction of the radiative recombination centers.

Layout of the thesis

The thesis consists of five chapters. The list of publications and conference contributions on the results summarized by this thesis are listed in the beginning of the thesis.

The first chapter, an overview of ZnSe scintillator parameters and the mechanisms of radiative recombination related to defects is provided.

In chapter 2, the experimental setups and parameters of the samples under study are described. Experimental techniques used include luminescence spectroscopy and PL decay in the time and frequency domains, measurements of absolute quantum yield, the NBE optical absorption, the scanning near-field optical microscopy, *in situ* proton-excited luminescence, and electron paramagnetic resonance.

Chapter 3 reports on the comparative analysis of photoluminescence spectra in different ZnSe crystals doped with isoelectronic tellurium, oxygen, and oxygen with aluminum impurities, and annealed or unannealed in Zn vapor; the study of temperature dependence of the defect-related PL spectra in annealed ZnSe(Te), ZnSe(O), ZnSe(O,Al), and ZnSe under band-to-band (at the crystal surface) and two-step (in the crystals bulk) excitation conditions is presented; thermal ionization energies of donor and acceptor are estimated; phonon energies, for the both low-energy and high-energy luminescence bands in different samples are estimated; the numerical simulation of the defect-related PL intensity dependence on temperature is performed, and the decay kinetics are presented and discussed; numerical simulation of PLE spectra of LE PL band and evaluation of electron-phonon interaction strength in the different crystal is evaluated.

In chapter 4, the influence of co-doping by rare earth oxides on the PL efficiency is discussed; the results of numerical simulation of the decay kinetics at a high excitation level (in the time domain) and at a low excitation level (in the frequency domain) are presented; experimental study and the simulation of the dependence of absolute quantum yield on excitation photon energy is presented and discussed; the origin of the decrease in efficiency of the defect-related luminescence in ZnSe(Te) is revealed; the effective charges of tellurium- and oxygen-related complex defects are evaluated.

Chapter 5 reports on *in situ* study of luminescence spectra and nonequilibrium carrier transients in conventional ZnSe(Te) scintillator irradiated with 1.6 MeV protons

under different fluences; evaluation of the radiation defects generation rate, and on peculiarities of nonequilibrium carrier recombination mechanisms under excitation by protons and visible light are discussed.

Chapter 2. Experimental

2.1. Photoluminescence decay kinetic measurement setup

2.1.1 Time-resolved and steady-state PL spectroscopy

The steady-state PL studies under band-to-band excitation conditions were performed using CW excitation by He-Cd laser radiation at 3.81 eV (325 nm) and maximal power density of ~1.5 W/cm^2. The temperature was changed in the range from 8 to 300 K using a closed-cycle helium cryosystem. The measurements were performed in the single photon counting regime by using single-photon counter.

To avoid the influence of the nonradiative surface recombination, the carriers were generated in the crystal bulk using two-step excitation. The measurements of PL decay kinetics and PL spectra under two-step excitation condition (the results in Chapter 3) were performed by using the second harmonic of Q-switched YAG:Nd^{3+} laser radiation. The excitation photon energy of 2.33 eV (532 nm) was well below the band gap of the samples under study and the carrier were generated via two-step (or two-step) excitation. The excitation power density was set at 3 MW/cm^2. The two-step excitation was selected to avoid the influence of surface recombination, which is more pronounced at strong band-to-band absorption resulting in a short absorption depth (typically ~100 nm). The PL signal was analyzed using a 0.6 m double monochromator (*Jobin Yvon* HRD-1) and detected by a photomultiplier tube (Hamamatsu R1463P) and a box-car integrator. The PL decay and TRPL spectra were measured with the time resolution of ~0.3 μs by changing a delay between the excitation pulse and the triggering pulse for the box-car integrator. A closed-cycle helium cryosystem was used to perform the measurements in a wide temperature range from 8 to 300 K.

Photoluminescence studies of the crystals co-doped by rare earth oxides, which are reported in Chapter 4, were performed at excitation photon energy of 2.58 eV (480 nm), which is also below the ZnSe band gap ($E_g = 2.7$ eV). This excitation condition was realized by using the emission of the pulsed optical parametric oscillator (*EKSPLA* NT342B, pulse duration 4 ns, maximal excitation power density 9 MW/cm^2). The photoluminescence was detected and analyzed using ICCD camera (*Andor iStar* 320T*)* coupled with a spectrometer (*Andor Shamrock* SR-500i). The PL study in time domain (TD) was accomplished by changing the delay between the excitation and PL pulses in the range from nanoseconds to milliseconds.

The X-ray luminescence (XRL) spectra were measured using spectrometer *KSVU*-23 and photomultiplier *FEU*-100. X-ray source *REIS-I* ($U_a = 20$ kV, $i_a = 25$ μA, copper anode) was used for excitation. The measurements of XRL spectra were performed at room temperature.

2.1.2 The FDLM measurement technique

The frequency domain luminescence lifetime measurement (FDLM) technique [1] was used to study the PL decay kinetics at low excitation levels (down to 3 mW/cm^2). The emission of an LED peaking at 2.64 eV (470nm) was used for PL excitation in FDLM experiments. The LED emission intensity was modulated in the frequency range from 1 Hz to 250 kHz. As a result, the photoluminescence response was also modulated at the same frequency. Due to a finite luminescence decay time, the detected luminescence signal had a phase shift and its modulation depth was lower. A Fourier transform of the experimentally obtained frequency dependence of the phase shift enables one to recover any luminescence decay function. All the FDLM measurements in this study have been performed at room temperature.

2.2. Measurements of the absolute quantum yield

The absolute quantum yield (QY) was measured at room temperature using an integrating Ulbricht sphere [2] (*SphereOptics*). To measure the wavelength dependence of QY and selectively excited PL spectra, a halogen lamp was used together with a monochromator (*Jobin Yvon* H-10) for tunable-wavelength excitation (excitation power density ~1-10 μW/cm^2).

2.3. Setup for study of NBE optical absorption

The measurements of optical transmission spectra of the crystals having the thickness of 0.5 mm and 2 mm were performed to calculate the absorption spectra according to relation $\alpha = \ln(T_1 / T_2) / d_2 - d_1$, where $T1$ and $T2$ are transmissions and d1, d2 are thickness of the two samples under study, respectively. Monochromated emission (monochromator *LOMO* MDR- 23) of halogen lamp was transmitted through the sample under study and then registered by a germanium photodiode. To increase the signal-to-noise ratio lock-in amplifier (*Stanford Reseach System* SR530) and light chopper were used.

2.4. Confocal microscope setup for spatially resolved spectroscopy

The spatially-resolved PL study has been performed using *WITec* microscopic system *Alpha* 300 S operated in confocal mode. The microscope was coupled by an optical fiber with a *Cromex* spectrometer. A CW semiconducting laser (*ALPHALAS*) emitting at 3.05 eV (405 nm) was used for excitation. Objective (*Nikon*) with numerical aperture NA = 0.9 was used to ensure the lateral resolution of ~200 nm. Measurements in SNOM mode ensured spatial resolution of ~260 nm, which was limited by the aperture of the tip used. All the measurements have been carried out at room temperature.

2.5 Setup for *in situ* study of variations of proton induced luminescence

In situ study of the variation of luminescence excited with protons were performed in the Nuclear and environmental radioactivity research laboratory at the Institute of

Physics [3]. The proton beam was accelerated in the *Tandetron* 4110A ion accelerator up to the energies of 1.6 MeV. To reduce the channeling effect, the proton propagation path was slightly modulated.

The measurements were performed in three experimental configurations. Initially, the study of luminescence and photoconductivity characteristics were performed in non-irradiated ZnSe(Te) samples. The nonequilibrium carriers were photoexcited within a spot of a 3.1×10^{-2} cm^2 in area using the harmonics of the emission of microchip laser STA-1-TH (pulse duration 500 ps, repetition rate 100 Hz). The MW-PC transients were recorded either under excitation below the ZnSe band gap (using bulk excitation at a photon energy of 2.33 eV) and under band-to-band excitation (a surface excitation regime at 3.50 eV (354 nm)). The MW-PC response was detected by a coaxial needle-tip probe in a near-field probing regime using the measuring device VUTEG fabricated at Vilnius University [4]. A microwave reflection mode has been exploited in these measurements. The processed signal was transferred from the VUTEG detection system to a digital 1 GHz oscilloscope *Tektronix* TDS-5104 equipped with a computer, where the MW-PC transients were displayed and analyzed. The luminescence excited by the laser emission was collected from the front surface of the sample. The laser light was filtered out by a selective mirror. The luminescence signal was guided to the monochromator input slit using a fiberscope with an aperture of 3×10^{-2} cm^2 in area. The time-resolved PL transients are recorded by using a *ScienceTech*-9030 monochromator equipped with a *Hamamatsu* H-10721-20 photodetector. The output of this fast photodetector (time resolution of 1 ns) enabled displaying the luminescence decay at a fixed wavelength.

The spectra of the proton-induced luminescence (PI-L) and the transients of the microwave probed photoconductivity (MW-PC) were recorded simultaneously. During the *in situ* measurements, the sample was mounted on a cold finger within a specially fabricated irradiation chamber [5,6]. Special coaxial and fiber connectors mounted in the chamber were used to transfer the optical and microwave signal to the measurement setup located remotely from the irradiation area. The irradiation chamber was also equipped with 3D actuators to adjust the proton beam location on the sample. The MW-PC transients and quasi-steady-state PI-L signals were synchronously recorded during exposure to the proton beam. The PI-L signal was integrated over $\tau_{PL\text{-}av}$ = 300 ms using a photometer *Avantes AvaSpec*-2048TEC. Post-irradiation experiments were used to determine more precisely the stopping range for the 1.6 MeV protons and to emulate the procedure of the signal collection and averaging from the inhomogeneously damaged sample volume. The profiles of the MW-PC response have been scanned by varying the position of the sharply focused laser beam intersecting with the microwave probe antenna on the side wall of the sample. Simultaneously, the photoluminescence excited by the laser beam at different distances from the front surface of the sample was collected through the front surface of the sample [7]

2.6. Setup of electron paramagnetic resonance study

The electron paramagnetic resonance (EPR) measurements were carried out using an X-band spectrometer (*Bruker Elexsys* E580) operating in microwave frequency range from 8 to 10 GHz. A programmable goniometer (E218-1001) was used for the rotation of samples with respect to the external magnetic field. The samples were cooled down to

90 K using a continuous nitrogen gas flow from *Bruker* cryostat. The resonance microwave frequency and relevant microwave power (varied in the range of 0.2-2.4 mW) were changed to find the undistorted EPR signal.

2.7. Objects under study

The crystals under study were grown by the Bridgman-Stockbarger technique. The growth in a graphite crucible in a vertical compression furnace under argon pressure of 5×10^6-1×10^7 Pa and the temperature of 1800-1900 K ensured the growth rate of 5-7 mm/h. Mechanically-enhanced oxygen ion implantation into the host ZnSe lattice has been accomplished by grinding raw ZnSe, annealing the finely ground powder in an oxygen-rich atmosphere and re-melting the oxygen-rich ZnSe powder for further regrowth of monocrystals containing oxygen. Hereafter, the samples are denoted as ZnSe(O). Alternatively, oxygen has been introduced by adding 0.03-0.1 wt% of Al_2O_3 into the charge for growth of ZnSe monocrystals. As a result, the crystals grown this way were co-doped with oxygen and aluminum; denoted as ZnSe(O,Al). Conventional ZnSe(Te) scintillator monocrystals with 1 wt% tellurium concentration in the charge were grown for comparison. Co-doping by the rare earth elements has been accomplished by introducing Ce_2O_3 or Sm_2O_3 compounds into the melt for growing ZnSe-based scintillator monocrystals. All the crystals under study were annealed in Zn vapor under 1 atm at 1200-1300 K temperature for 72 hours.

Chapter 3. Defect-related luminescence in isoelectronically-doped ZnSe crystals

3.1 Influence of isoelectronic impurities and annealing in Zn vapor on the properties of defect-related luminescence

3.1.1 Spectra of defect-related luminescence

The normalized CW defect-related photoemission spectra measured under band-to-band excitation in isoelectronically doped ZnSe(Te) and ZnSe(O,Al) crystals are shown in Fig. 3.1.1.1. Both unannealed samples and samples annealed in zinc vapor (indicated as ZnSe(Te) and ZnSe(Te):Zn, respectively) were studied.

The thermal treatment of the ZnSe crystals annealed in Zn vapor increases the intensity of the spectrally-integrated PL approximately by a factor of 3 in all isoelectronically doped ZnSe samples under study. Meanwhile, the enhancement factor in undoped ZnSe is only 1.3 at the band-to-band excitation condition. Annealing of ZnSe and ZnSe(Te) results in an enhancement of the low energy part of the composite band, while the emission in the high energy side of the band is suppressed. On the contrary, the annealing of ZnSe(O,Al) has no significant effect on its PL spectrum shape.

The analysis of the nature of the spectral changes in PL of the ZnSe monocrystals under study was performed by deconvolution of the PL spectra using Alentsev-Fok deconvolution procedure [8]. The deconvolution procedure was accomplished by comparing the PL spectra of the annealed ZnSe samples with those in the unannealed ZnSe samples. The deconvoluted PL spectra of annealed and unannealed ZnSe(Te) and

ZnSe(O,Al) samples are shown in Fig. 3.1.1.1 (a) and (b), respectively. The decomposition of the PL spectra in ZnSe(O) and undoped ZnSe was performed similarly.

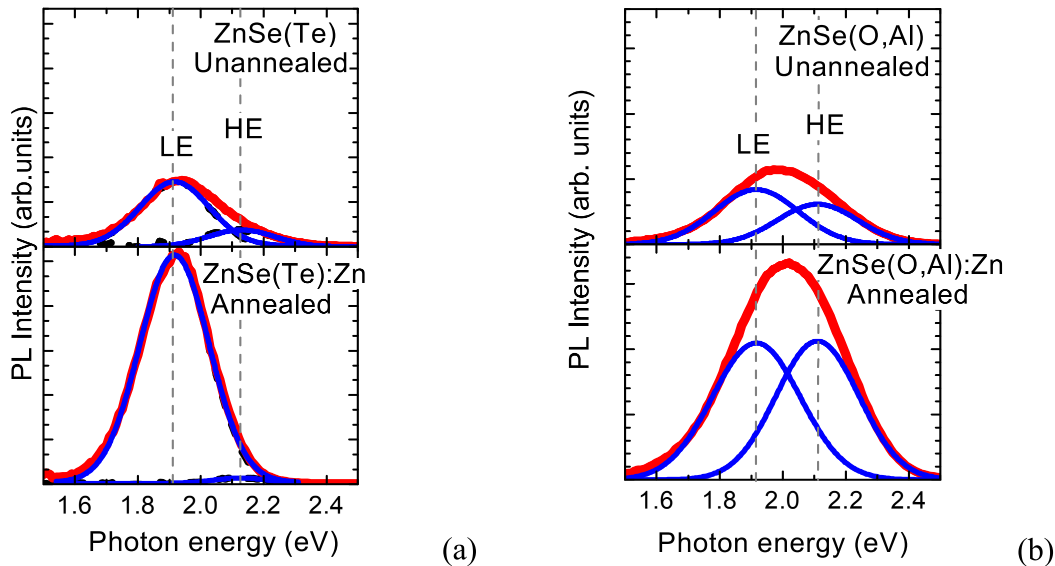

Fig. 3.1.1.1. PL spectra measured in annealed and unannealed ZnSe(Te) (a) and ZnSe(O,Al) (b) (red lines). Deconvoluted spectral components are depicted by blue solid curves.

The Low-energy PL band is peaked at 1.92 eV in all the ZnSe crystals under study at band-to-band excitation conditions at room temperature. The emission peak of the HE band slightly varies in the range from 2.11 eV to2.13 eV in different samples.

Annealing of different ZnSe crystals in Zn vapor has different effect on the shape of their PL spectra. Thus, the crystals can be classified in two groups. For the first group, annealing in Zn vapor suppresses the HE band and enhances the LE PL band and the latter becomes dominating in the annealed crystal. This behavior is inherent to ZnSe(Te) and intentionally undoped ZnSe samples. For the second group, annealing enhances the intensity of both LE and HE PL bands in ZnSe(O) and ZnSe(O,Al) (see Table 3.1.1.1.).

Table 3.1.1.1. PL peak position, FWHM and intensities of deconvoluted LE and HE bands (see Fig. 3.1.1.1).

<table>
<tr><th rowspan="2"></th><th colspan="2">Peak(eV)</th><th colspan="2">FWHM (eV)</th><th colspan="2">Intens. (arb.u.)</th></tr>
<tr><th>LE</th><th>HE</th><th>LE</th><th>HE</th><th>LE</th><th>HE</th></tr>
<tr><td>ZnSe(Te)</td><td rowspan="8">1,92</td><td rowspan="2">2.13</td><td rowspan="2">0.259</td><td>0.250</td><td>120</td><td>30</td></tr>
<tr><td>ZnSe(Te):Zn</td><td>0.214</td><td>430</td><td>10</td></tr>
<tr><td>ZnSe(O)</td><td rowspan="2">2.12</td><td colspan="2" rowspan="2">0.240</td><td>87</td><td>60</td></tr>
<tr><td>ZnSe(O):Zn</td><td>320</td><td>120</td></tr>
<tr><td>ZnSe(O,Al)</td><td rowspan="4">2.11</td><td>0.313</td><td>0.300</td><td>1400</td><td>980</td></tr>
<tr><td>ZnSe(O,Al):Zn</td><td>0.327</td><td>0.31</td><td>3650</td><td>3490</td></tr>
<tr><td>ZnSe</td><td rowspan="2">0.252</td><td rowspan="2">0.271</td><td>26</td><td>7</td></tr>
<tr><td>ZnSe:Zn</td><td>40</td><td>4,8</td></tr>
</table>

The LE and HE PL bands have been observed in numerous papers before. The results obtained by ODMR [9,10,11,12] evidence that both bands are caused by

recombination in donor-acceptor pairs (DAP) and indicate coexistence of donors and acceptors in close proximity. The results obtained by PL and photoinduced absorption spectroscopy showed that the complexes responsible for the LE band in ZnSe(Te) might have the form $\{V_{Zn}^{-} + Te_{Se}^{0} + D^{+}\}^{0}$ [13], while the HE band might be caused by recombination via complexes $\{V_{Zn}^{-} + D^{+}\}^{0}$ [14]. Annealing is favorable for formation of the LE band, since a Te atom, being larger than a Se atom, partially compensates the lattice distortion due to Zn vacancy. Consequently, the complex $\{V_{Zn}^{-} + Te_{Se}^{0} + D^{+}\}^{0}$ is more stable than the complex $\{V_{Zn}^{-} + D^{+}\}^{0}$ [14]. On the other hand, oxygen atoms are smaller than selenium atoms. However, they might stabilize the $\{V_{Zn}^{-} + O_{Se}^{0} + D^{+}\}^{0}$ complexes in ZnSe(O) due to their higher electronegativity.

It is believed, that redistribution of the emission intensity between LE and HE bands in favor of LE band during the annealing is caused by healing of Zn vacancies in $\{V_{Zn}^{-} + D^{+}\}^{0}$ complex. Thus, the donors released from these complexes take part in formation of the defect complexes $\{V_{Zn}^{-} + Te_{Se}^{0} + D^{+}\}^{0}$, which are more stable in the annealing process [13,14].

Aluminum in ZnSe can form donor states [15,16] and, at high doping levels, can cause a high density of free electrons [17]. The Al ion can also occupy zinc vacancy. Interaction of such substitutional Al_{Zn} defects with neighboring Zn vacancies leads to the formation of A-type centers $\{V_{Zn}^{-} + Al_{Zn}^{+}\}^{0}$ which have been evidenced in ZnS [18] and ZnSe [19,20]. The introduction of aluminum might affect the defect-related emission in ZnSe(O,Al) by entering into the defect complexes as a donor as well as by forming a shallow hydrogen-like donor [21].

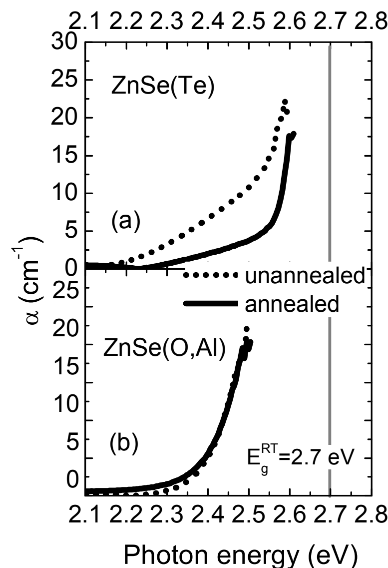

Fig. 3.1.2.1 . Near-band-edge optical absorption in ZnSe(Te) (a) and ZnSe(O,Al) (b) annealed (solid curves) and unannealed (dotted curves) in Zn vapor. T = 295 K.

3.1.2 Near-band-edge optical absorption in annealed crystals

It was established, that the thermal treatment of ZnSe in Zn vapor enables one to purify the crystals from the electrically and optically active residual impurities serving as donors (Al, In, etc.) or acceptors (Cu, Ag, etc.) in the band gap [22]. The annealed crystals become highly-conductive n-type or even degenerate because of high density of interstitial Zn_i [23,24,25].

The Figure 3.1.2.1 shows the NBE optical absorption spectra of annealed and unannealed ZnSe(Te) and ZnSe(O,Al) crystals at room temperature.

The absorption in annealed ZnSe(Te) is shifted to the high energy side relative to that in unannealed ZnSe(Te). The same tendency was observed in ZnSe(O) and undoped ZnSe (not shown here). Meanwhile, annealing of ZnSe(O,Al) sample does not cause significant changes in NBE absorption. It might be assumed, that the blueshift of NBE absorption in annealed ZnSe(Te) (as well as in ZnSe and ZnSe(O)) occurs due to healing of zinc vacancies and purification of residual impurities from the crystal bulk. Note, that

annealing in Zn vapor also causes redistribution of PL spectra in ZnSe(Te) and ZnSe. Thus, it can be assumed that an optical transition involving residual donor-like impurities (Al, In, etc.) or interstitial Zn_i and isoelectronic oxygen-related complex results in 2.1 eV PL band. Since the 1.92 eV PL band is effectively intensified by both tellurium and oxygen. Thus, it might be assumed that LE and HE bands are different in their nature.

3.1.3 Effect of annealing in Zn vapor on photoluminescence and photoconductivity transients

The transients of MW-PC and the defect-related PL of annealed and unannealed ZnSe(Te) and ZnSe(O,Al) crystals are shown in Fig. 3.1.3.1. The two-step excitation by 2.33 eV pulsed laser emission was employed to excite nonequilibrium carrier in the crystals bulk. To compare, the transients were fitted using biexponential function. The fitting parameters are listed in Table 3.1.3.1.

The MW-PC transients of the crystals doped with oxygen or oxygen and aluminum are faster than those in ZnSe and ZnSe(Te). Both fast, τ_1, and slow, τ_2, components of MW-PC transients become slower in the annealed ZnSe crystals. Note that the MW-PC transient of the annealed ZnSe(O,Al) contains a slow (310 μs) intense component, which is absent in the unannealed ZnSe(O,Al). This is an indication of a high density of the electron traps in band gap of annealed ZnSe(O,Al) scintillation crystals.

Both PL decay components become faster after the annealing of ZnSe(Te) and ZnSe(O,Al) crystals. Annealing of ZnSe(O) and ZnSe shows a more complicated trend: the initial decay becomes faster, whereas the other decay component becomes slower.

The annealing-induced changes of PL and MW-PC transients might be attributed to redistribution of the density of states in the band gap. The photoluminescence efficiency enhancement in the annealed ZnSe crystals under study evidences the “healing” effect on the lattice defects serving as centers of nonradiative recombination and carrier traps.

The absolute quantum yield of the annealed ZnSe crystals exceeds that of the unannealed crystals by a factor of 5-100 in different crystals (see the Table 3.1.3.2).

Table 3.1.3.1. Decay constants (in μs) for MW-PC, τ_{PC}, and PL, τ_{PL}, transients in crystals annealed and unannealed isoelectronically doped ZnSe (Fig. 3.1.3.1)

<table>
<tr><th colspan="2"></th><th colspan="2">ZnSe(Te)</th><th colspan="2">ZnSe(O)</th><th colspan="2">ZnSe(O,Al)</th><th colspan="3">ZnSe</th></tr>
<tr><th colspan="2"></th><th>τ_1</th><th>τ_2</th><th>τ_1</th><th>τ_2</th><th>τ_1</th><th>τ_2</th><th>τ_1</th><th colspan="2">τ_2</th></tr>
<tr><td rowspan="2">Annealed</td><td>τ_{PC}, μs</td><td>25</td><td>141</td><td>7</td><td>30</td><td>7</td><td>310</td><td>5</td><td colspan="2">146</td></tr>
<tr><td>τ_{PL}, μs</td><td>16</td><td>52</td><td>15</td><td>48</td><td>1.7</td><td>6.5</td><td>31</td><td colspan="2">127</td></tr>
<tr><td rowspan="2">Unannealed</td><td>τ_{PC}, μs</td><td>7,2</td><td>37,7</td><td>0,55</td><td>25,3</td><td>4,8</td><td>97</td><td>2,5</td><td>12,1</td><td>80,6</td></tr>
<tr><td>τ_{PL}, μs</td><td>25</td><td>226</td><td>2.2</td><td>11.6</td><td>6</td><td>42</td><td>2.9</td><td>15</td><td>--</td></tr>
</table>

Table 3.1.3.2. The highest QY in different isoelectronically doped ZnSe samples annealed and unannealed in Zn vapor.

	ZnSe(Te)	ZnSe(O)	ZnSe(O,Al)	ZnSe
Annealed	21.5%	11.5%	11.5%	9%
Unannealed	4.7%	0.1%	2%	0.1%

In conclusion, the defect-related PL in all the crystals under study involves the two different channels of the carriers radiative recombination. Annealing ZnSe(Te) and ZnSe

suppresses the 2.1 eV PL band, so that the 1.92 eV PL band dominates at room temperature (fractional intensity is more than 90 %). Meanwhile, the spectra of ZnSe doped with oxygen or oxygen and aluminum are complex and consist of two strongly overlapping PL bands peaked at ~1.92 eV and ~2.1 eV.

Annealing of the crystals in Zn vapor suppresses the channels of nonradiative recombination and enhances scintillation efficiency of ZnSe crystals by a factor of ~5 in ZnSe(Te) and ZnSe(O,Al) and by a factor of 100 in ZnSe(O) and intentionally undoped ZnSe.

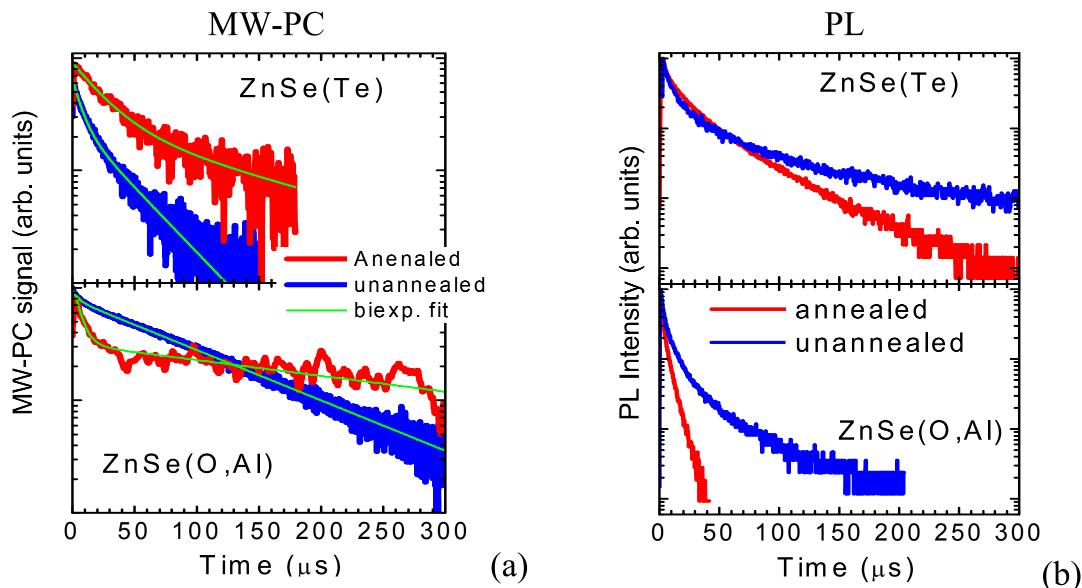

Fig. 3.1.3.1 . MW-PC (a) and PL (b) transients in ZnSe(Te) and ZnSe(O,Al) annealed (red curves) and unannealed in Zn vapor (blue curve).

3.2 Temperature dependence of defect-related PL spectra in annealed ZnSe crystals

3.2.1 Carrier generation at the crystal surface under band-to-band excitation

The photoluminescence spectra of ZnSe(Te) and ZnSe(O,Al) measured in the temperature range from 8 to 300 K at band-to-band CW excitation (3.81 eV) are shown in Fig. 3.2.1.1(a) and (b), respectively. It was observed that the PL spectra in ZnSe(Te), ZnSe(O), and undoped ZnSe at different temperatures are similar (not shown in Fig. 3.2.1.1).

The PL spectra in all the samples consist of two overlapping bands of different origin. The photoemission in the range from 2.4 to 2.8 eV is related to the NBE PL band, while the luminescence band in the range from 1.6 to 2.4 eV is attributed to defect-related photoemission. Spectrally integrated intensity of NBE and defect-related emission in ZnSe(Te) is the same at 8 K temperature under band-to-band excitation. This is an indication that equal parts of the excess carrier density in ZnSe(Te) (as well as in ZnSe(O) and ZnSe) recombine via shallow and deep levels in the band gap at 8 K under band-to-band excitation. However, the NBE PL band in ZnSe(O,Al) is suppressed and its intensity is lower by nearly three orders of magnitude. The suppression of NBE emission might be caused by different factors: i) screening of shallow impurities by

nonequilibrium carrier plasma [26], ii) shallow impurity might be thermally ionized even a 8 K due to reduction of thermal ionization barrier, provided that the density of impurity is quite high (after Debye and Conwell model [27,28]), iii) impurities tend to form defect complexes or impurity clusters [29,30]. The next discussion will be focused on the properties of the defect-related PL.

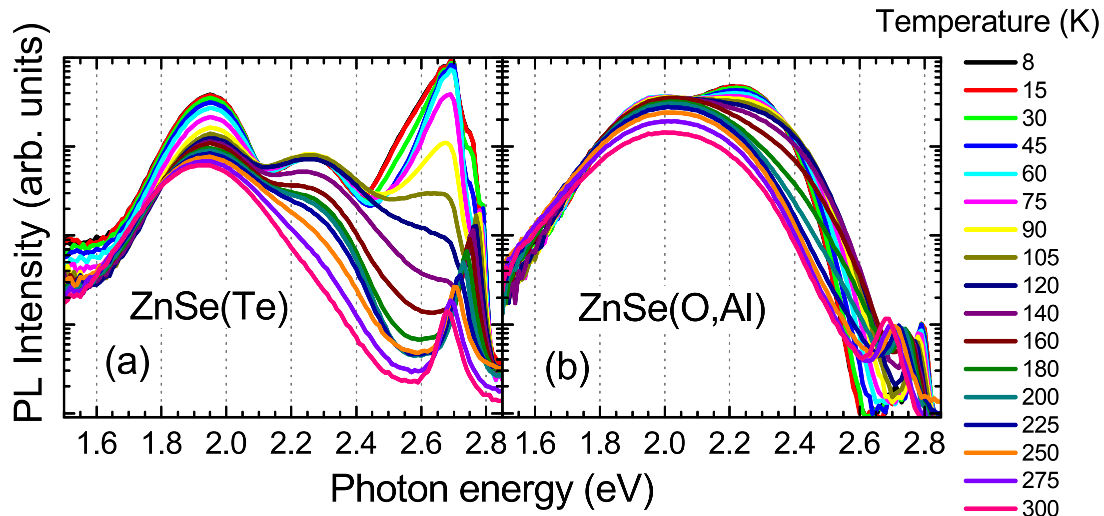

Fig. 3.2.1.1. PL spectra of annealed ZnSe(Te) and ZnSe(O,Al) measured in temperature range from 8 to 300 K under CW excitation by He-Cd laser emission (3.81 eV), under excitation power density of 1.5 W/cm^2.

The defect-related PL is complex and its spectrum consists of two strongly overlapped PL bands peaked at ~1.95 and ~2.25 eV, LE and HE bands, respectively. Intensity of the HE band shows no considerable temperature dependence at temperatures below ~120 K, but its intensity drastically drops in all the samples under study at elevated temperatures. Note, however, that at lower temperatures, the HE PL band in ZnSe(O,Al) is more pronounced than the LE band. The integrated intensity of LE band in ZnSe(Te) (the trends in ZnSe(O) and ZnSe are similar) is by a factor of ~4 higher than that of HE band. Meanwhile, the integrated intensity of both LE and HE PL bands in ZnSe(O,Al) is approximately identical.

The temperature dependence of the spectra was analyzed by fitting the defect-related PL with two Gaussians. The best fit for PL spectrum of ZnSe(O,Al) at 8 K is shown Fig. 3.2.1.2. The fitting procedure was performed as follows. At low temperatures (below ~160 K), where the PL bands are clearly distinguishable, the PL peaks were varied manually to get the best fit by the least-square method. At elevated temperatures both bands strongly overlap, thus, the fitting was performed by varying manually the PL peak position of both bands. The band intensity and FWHM were varied as free parameters.

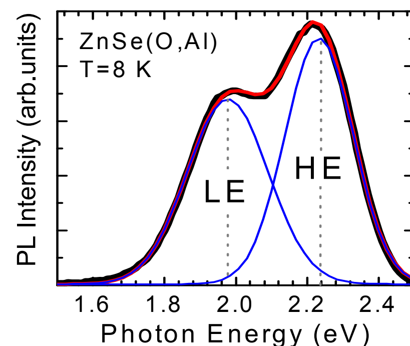

Fig. 3.2.1.2. The spectrum of ZnSe(O,Al) crystals at 8 K temperature (black curve), the blue curves corresponds to fit by the Gauss function, and red curve is sum of fitted curves.

Dependence of PL peak position on temperature

The temperature dependences of the PL peak position for LE and HE bands in annealed ZnSe(Te), ZnSe(O), ZnSe(O,Al), and ZnSe are plotted in Fig. 3.2.1.3.

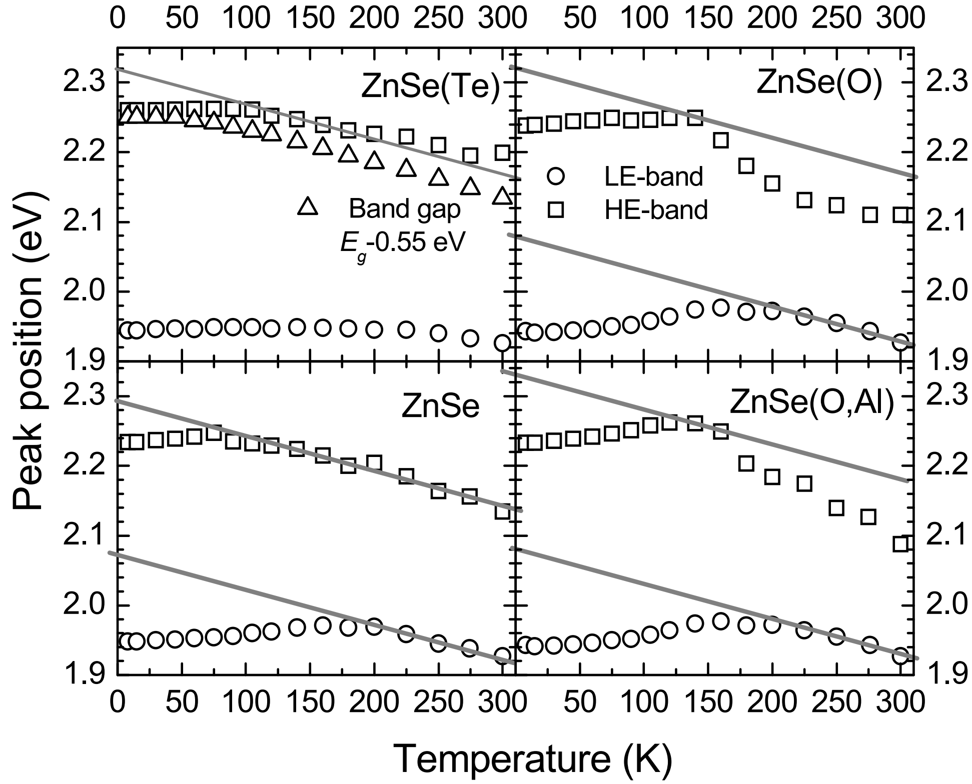

Fig. 3.2.1.3. Temperature dependence of PL peak positions of LE (circles) and HE (squares) bands in different ZnSe samples (indicated). Triangles correspond to band gap in ZnSe under study (downshifted by 0.55 eV). The temperature dependence of band gap (grey solid line) are shifted (as indicated).

The temperature dependence of LE and HE band positions shows a similar dependence by increasing temperature in all the samples under study. At lower temperatures, the PL peak shifts to the high energy side with increasing temperature and reaches its maximum value at a certain temperature T_{max}. The value of T_{max} for HE band is in the range from 75 to 150 K, and for LE band from 160 to 200 K in different ZnSe samples. Above T_{max}, the PL bands shift gradually to low energy side. This temperature dependence of PL peak position can be attributed to DAP luminescence and might be explained as follows [31]. At low temperature, well below T_{max}, the nonequilibrium carriers are captured by DAPs, and the energy of emitted photon in the DAP is $h\nu = E_g - E_a - E_d + J(r)$, where E_g is the band gap energy, E_a, E_d are thermal ionization energies of acceptor and donor, respectively, and $J(r)$ is the term of Coulomb interaction in the DAP. At increasing temperature, the shallower of the levels E_a and E_d (typically, it is the donor level in ZnSe) becomes ionized. Thus, the energy of emitted photon gradually shifts to the value of $h\nu = E_g - E_a$ by increasing temperature. The photon energy $h\nu = E_g - E_a$ corresponds to carriers recombination from CBM to acceptor level. Thus, at elevated temperatures, well above the T_{max}, the position of the luminescence peak is defined by the temperature-dependent shrinkage of the band gap (which in the samples under study proceeds at 0.45 meV/K). The temperature dependence of the band gap in ZnSe crystals under study is shown in Fig. 3.2.1.3 by the triangles (the dependence is shifted down by

0.55 eV). Figure 3.2.1.3 shows that the PL band peaks at elevated temperatures coincide with the band gap in ZnSe(Te) and ZnSe. The shift of HE band peak in the ZnSe(O) and ZnSe(O,Al) proceeds faster than the shrinkage of the band gap in ZnSe. It might be assumed that the more complicated temperature dependence of the PL peak in the oxygen-doped crystals might be caused by temperature instability of oxygen-related defect complexes. This assumption is indirectly confirmed by a very high diffusivity of oxygen in ZnSe, which exceeds that for tellurium by approximately 5 orders of magnitude. The corresponding diffusion coefficient at 1300 K is $\sim 8\times 10^{-6}$ cm^2/s and $\sim 6\times 10^{-11}$ cm^2/s for oxygen [32] and tellurium [33], respectively. The LE PL band behaves with increasing temperature similarly to HE band.

The thermal ionization energy of donor and acceptor can be evaluated from PL peak dependence on temperature. To estimate the term $E_d + J(r)$), the photon energy corresponding to DAP recombination should be subtracted from the photon energy corresponding to e - A transition. The energy of photon emitted in DAP is assumed to be equal to the PL peak of HE and LE band at 8 K. The photon energy corresponding to e - A transition is determined asymptotically continuing the slope of the PL band peak dependence on temperature at elevated temperatures to intersect the Y axis, as shown by the grey solid lines in Fig. 3.2.1.3. Then, the acceptor thermal ionization energy can be estimated. The estimated thermal ionization energies of donor and acceptor in all the ZnSe crystals under study are listed for LE and HE PL bands in Table 3.2.1.1.

The energies listed in Table 3.2.1.1 correspond to ionization of excited donor and acceptor. The ionization energy of deep acceptor in different crystals is ~0.5 eV for HE band, while the ionization energy of acceptors responsible for LE band is higher. The values of estimated ionization energies are in consistence with the energies reported in other papers: from ~0.4 [34,24] to 0.6 eV [13,10,35] for acceptor related to HE band and from 0.6 to 0. 75 [13,34,24,35,11,36] for acceptors related to LE-band. Many different donor levels located in the range from 0.03 to 0.37 eV below CBM are reported as possible candidates for the donor states in the DAP [9,10,12,24, 36,34].

Note, that the ionization energies in ZnSe(Te) is close to those in undoped ZnSe. Meanwhile, doping by oxygen or oxygen and aluminum reduces the energy of acceptor level and increases the energy of donor level, in respect to those in undoped ZnSe.

Table 3.2.1.1. Thermal ionization energies at the centers responsible for LE ir HE PL bands at 8 K temperature (see Fig. 3.2.1.3).

	E_g, eV	„e-A“, eV	„D-A“, eV	$E_d + J(r)$, eV	E_a, meV
HE band					
ZnSe(Te)	2.820	2.316	2.260	**0.056**	**0.5**
ZnSe		2.287	2.234	**0.053**	**0.53**
ZnSe(O)		2.323	2.235	**0.09**	**0.5**
ZnSe(O,Al)					
LE band					
ZnSe(Te)	2.820	2.069	1.944	**0.125**	**0.75**
ZnSe			1.948	**0.12**	**0.75**
ZnSe(O)		2.073	1.943	**0.13**	**0.75**
ZnSe(O,Al)		2.114	1.977	**0.14**	**0.71**

Dependence of FWHM on temperature

The temperature dependence of FWHM for both HE and LE PL bands is plotted in Fig. 3.2.1.4.

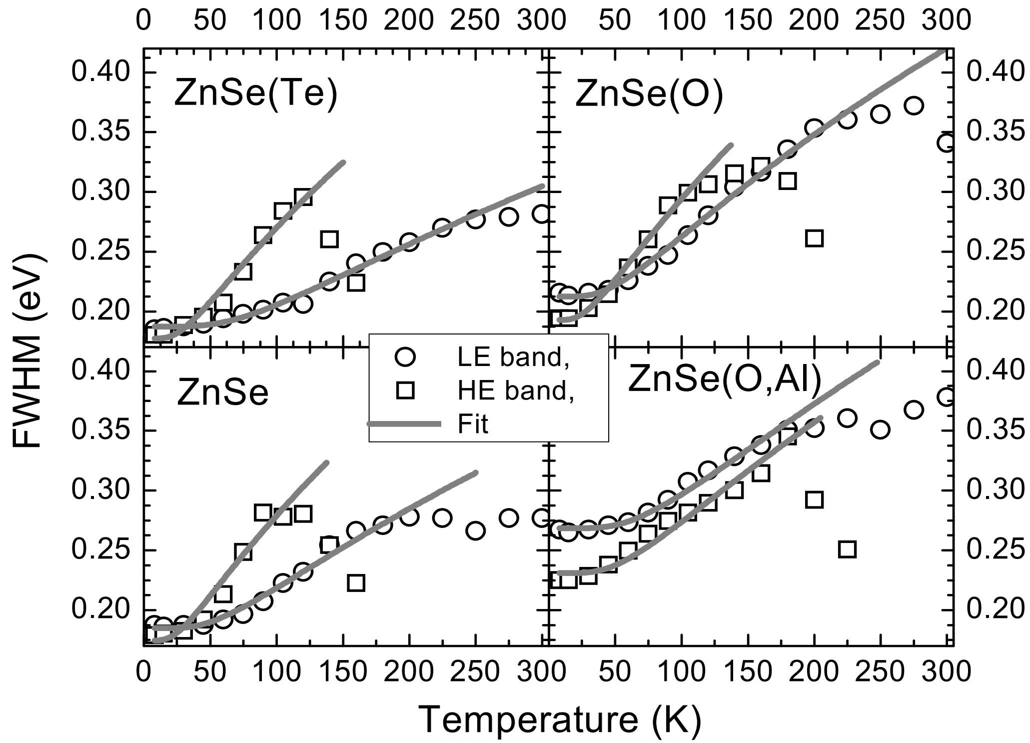

Fig. 3.2.1.4. FWHM dependence on temperature for LE (circles) and HE PL (squares) bands for different samples (indicated).

At low temperatures the FWHM of both HE and LE band increases with increasing temperature. At temperatures below ~150 K, the rate of the temperature-induced broadening of HE band is considerably faster than that of LE band. When the temperature reaches the value when the carriers primarily recombine from CBM to acceptor level, FWHM of HE band drastically drops. The widths of LE and HE bands in ZnSe(Te) and ZnSe are similar at the lowest temperature. Meanwhile, both PL bands are considerably broadened in ZnSe(O) and ZnSe(O,Al) crystals.

The FWHM for Gaussian-shaped PL band was fitted by using equation [37]

$$L_e(T) = L_e(0) \cdot \left[\text{th}(\frac{\hbar\Omega_e}{2kT}) \right]^{-1/2} . \qquad (3.2.1.1)$$

Here, $L_e(0)$ is FWHM at T= 0 K, $\hbar\Omega_e$ is the energy of phonon emitted when relaxing to the ground state, k is the Boltzmann constant, and T is temperature. The best fits are plotted in Fig. 3.2.1.4 by solid lines. The fitting parameters are listed in Table 3.2.1.2.

Table 3.2.1.2. FWHM L_e(0 K)at 0 K and phonon energy $\hbar\Omega_e$ for LE and HE bands.

	ZnSe(Te)		**ZnSe**		**ZnSe(O)**		**ZnSe(O,Al)**	
	LE	HE	LE	HE	LE	HE	LE	HE
L_e(0 K), meV	187	177	185	175	212	193	268	230
$\hbar\Omega_e$, meV	20.6	7.9	15	7.3	13.5	7.9	19.8	15.4

For simplicity, in the next discussion the phonons responsible for LE and HE bands will be referred to as LE-phonon and HE-phonon, respectively. The energy of LE-phonon exceeds that of HE-phonon in all the ZnSe crystals under study. The energy of HE-phonon in ZnSe(O,Al) is higher by a factor of ~2 than that in other ZnSe crystals. Note, that the HE-phonon energy in ZnSe(Te), ZnSe, and ZnSe(O) is by factor of 4 lower than the energy of longitudinal optical phonon (LO-phonon) in ZnSe ($\hbar\Omega_{LO}$ = 31 meV). This suggests, that the impurity (-ies) corresponding for the HE PL band are weakly bound with the host lattice. It might be assumed that the defects related to HE PL band includes impurity bound at vacancies [38,39], the chemically active oxygen [40], or maybe bound at dislocations like in GaN [41].

Dependence of PL intensity on temperature

The Arrhenius plots of the temperature dependence of the PL intensity for LE and HE bands in the temperature range from 8 K to 300 K under band-to-band CW excitation ($h\nu_{\text{exc}}$ = 3.81 eV) is shown in Fig. 3.2.1.5 . The increase of the temperature from 8 to 300 K results in the PL intensity decrease by a factor of 6 and 2.5 in ZnSe(Te) and ZnSe(O,Al), respectively. The barrier for nonradiative recombination at the crystal surface was estimated by fitting the temperature dependence of PL intensity using expression $I(T) = I_0 / \left(1 + C\exp\left[-E_a/k_B T\right]\right)$. Here, I_0 is the PL intensity at T=0, E_a is the barrier for the nonradiative recombination to occur, $C = p_{nr0}/p_r$ is the parameter corresponding to the ratio of nonradiative to radiative recombination rates at T=0, k_B is the Boltzmann constant. The fitting parameters for the different samples are listed in Table 3.2.1.3.

Two terms for thermal quenching were observed for HE band in ZnSe(Te) and ZnSe. The potential barrier for nonradiative recombination at the crystal surface in LE band is lower compared with that for HE band, except that in ZnSe(O,Al). Note that the potential barrier for thermal quenching of LE band under bulk excitation is much higher, E_a^{bulk} = 0.7 eV [42], than that under surface excitation conditions (12-100 meV). The low energy for thermal quenching of LE band at the crystal surface might be caused by mechanical polishing and/or oxidation of the ZnSe crystal surface [43].

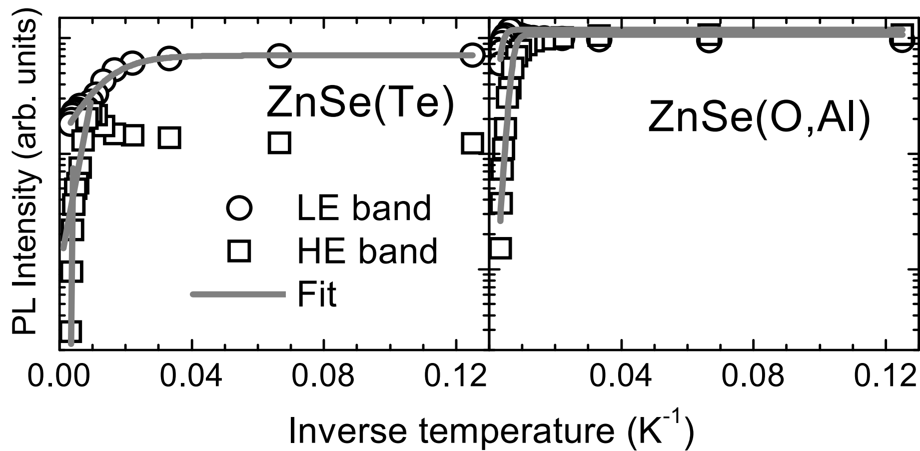

Fig. 3.2.1.5. The temperature dependence of the emission intensity of LE (circles) and HE (squares) bands measured under pulsed two-step excitation. Solid curves represent the Arrhenius dependence.

Table 3.2.1.3 . Thermal ionization energy E_a(meV) for HE and LE bands in different samples.

<table>
<tr><th></th><th>LE</th><th colspan="2">HE</th></tr>
<tr><td>ZnSe(Te)</td><td>12</td><td>56</td><td rowspan="2">170</td></tr>
<tr><td>ZnSe</td><td>23.5</td><td>53</td></tr>
<tr><td>ZnSe(O)</td><td>22.4</td><td colspan="2" rowspan="2">90</td></tr>
<tr><td>ZnSe(O,Al)</td><td>100</td></tr>
</table>

3.2.2 Carrier generation in crystals bulk under two-step excitation

To eliminate the carrier nonradiative recombination at crystal surface, the two-step excitation was employed by using 2.33 eV laser emission (pulse duration 4 ns) and excitation power density of 3 MW/cm^2. Photoemission spectra were recorded 0.1 μs after the excitation emission pulse. The spectra measured in ZnSe(Te) and ZnSe(O,Al) are presented in Fig. 3.2.2.1. The PL spectra in ZnSe(Te) are typical for ZnSe(O) and ZnSe, thus the last two are not presented.

The defect-related PL spectra measured under two-step excitation consist of two overlapping LE and HE bands and are similar to that measured under band-to-band excitation. Thus, in the following discussion, only the most significant differences to band-to-band excitation will be pointed out.

The analysis of the PL spectra was performed by fitting the spectra in LE and HE bands by double Gaussian. It was found, that the temperature dependence of the position of the defect-related PL band is complicated under the pulsed excitation condition. Thus, only the temperature dependences of FWHM and intensity were analyzed.

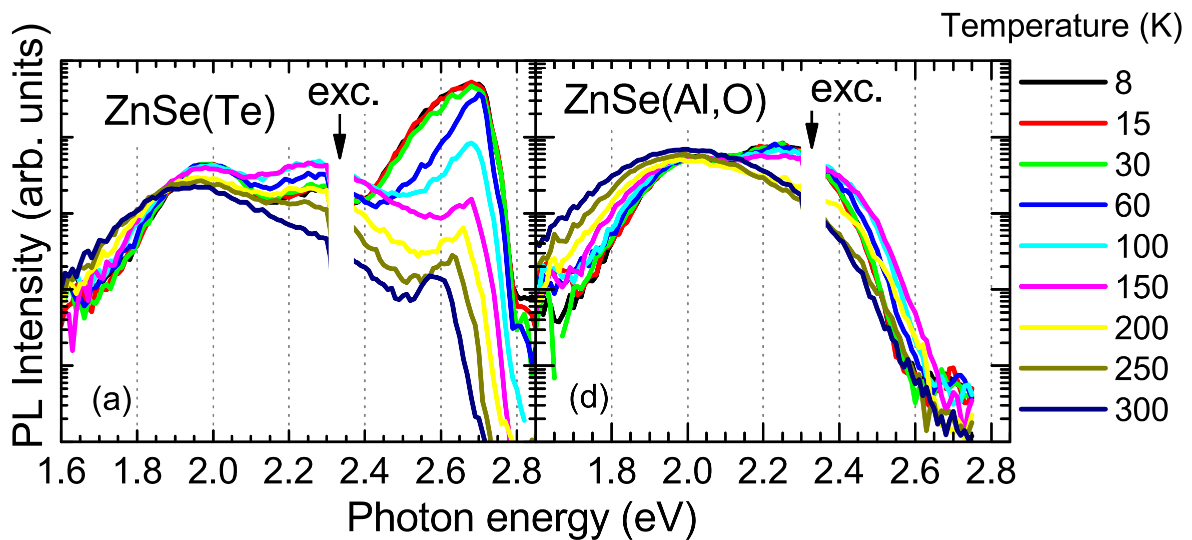

Fig. 3.2.2.1. PL spectra of ZnSe(Te) (a) ZnSe(O) (b), ZnSe (c), and ZnSe(O,Al) (d) scintillation crystals measured at different temperatures (indicated) under two-step excitation.

Temperature dependence of FWHM of defect-related PL under two-step excitation

The temperature dependence of FWHM for both HE and LE PL bands measured at two-step excitation condition is plotted in Fig. 3.2.2.2.

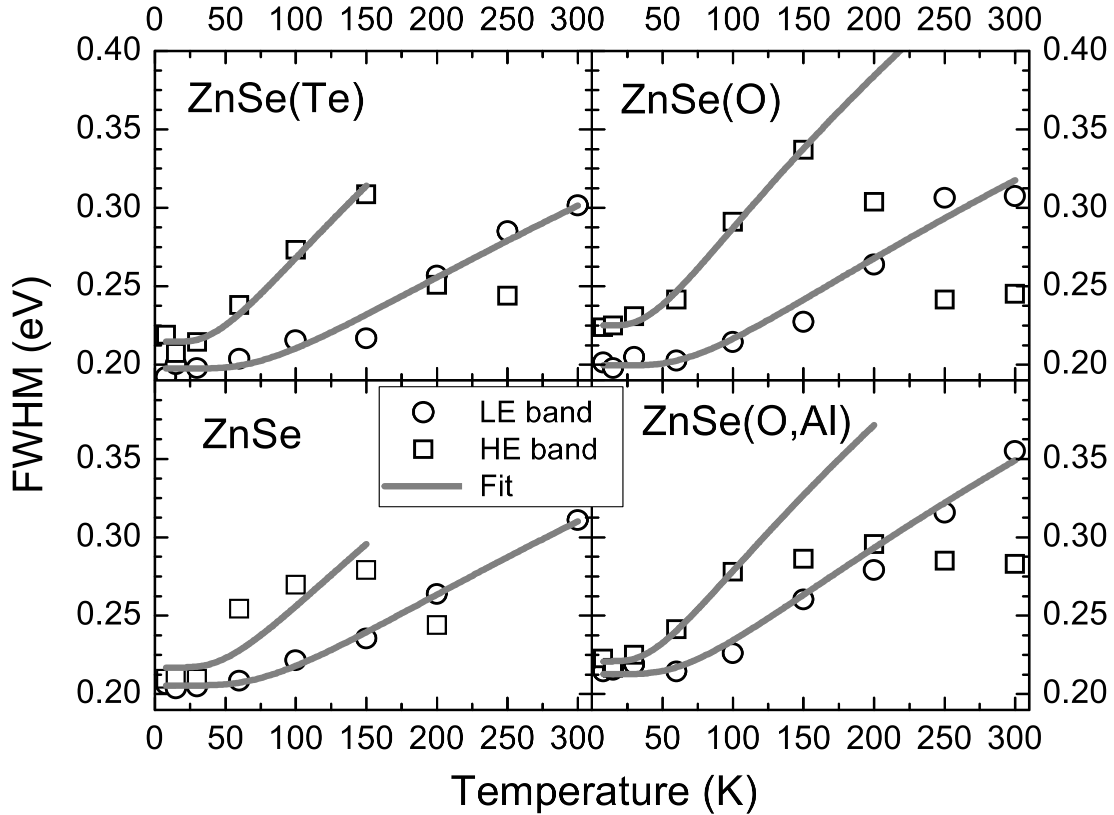

Fig. 3.2.2.2. FWHM dependence on temperature for LE (circles) and HE PL (squares) band in different ZnSe samples (indicated) at two-step excitation.

The FWHM temperature dependence for LE and HE PL bands was fitted using Eq. (3.2.1.1).The fitting parameters are listed in Table 3.2.2.1. The linewidths of LE and HE PL bands demonstrate similar temperature dependences as under band-to-band excitation. However, in ZnSe(Te) and undoped ZnSe under two-step excitation the FWHM of both PL bands is broadened considerably more than that under band-to-band excitation. Meanwhile, the oxygen-doped ZnSe crystals show an opposite trend and their PL bands are narrower.

The phonon energies for both PL bands increase in all the ZnSe crystals at carrier generation in the crystal bulk.

Table. 3.2.2.1. FWHM L_e(0 K)at 0 K and phonon energy $\hbar\Omega_e$, for the LE and HE PL bands at 8 K at two-step excitation condition.

	ZnSe(Te)		**ZnSe**		**ZnSe(O)**		**ZnSe(O,Al)**	
	LE	HE	**LE**	HE	**LE**	HE	**LE**	HE
L_e, meV	**197**	215	**206**	217	**200**	225	**213**	225
$\hbar\Omega_e$, meV	**23.7**	13.1	**24.4**	15.6	**21.6**	12.3	**20.2**	16.5

Temperature dependence of PL intensity under two-step excitation

The Arrhenius plots for LE and HE PL band intensity in the temperature range from 8 K to 300 K under pulsed two-step excitation ($h\nu_{exc}$ = 2.33 eV) are shown in Fig. 3.2.2.3

As is illustrated in Fig. 3.2.2.3, the intensity of the HE band shows no considerable temperature dependence at low temperatures, experiences an increase at elevated

temperatures, which is caused by the carrier redistribution between HE and NBE band, and drastically drops when the temperature exceeds 100 K. This behavior is qualitatively similar in all isoelectronically doped ZnSe crystals. However, enhancement of HE band intensity in low temperature range is less pronounced in ZnSe(O,Al), while its NEB emission is suppressed. The activation energy estimated for the drastic intensity drop at elevated temperatures is ~100 meV for different ZnSe samples (see the Arrhenius plot in Fig. 3.2.2.3). Note that the activation energy in ZnSe(Te) and ZnSe increases under two-step excitation in the crystal bulk by a factor of ~2 compared to that under band-to-band excitation.

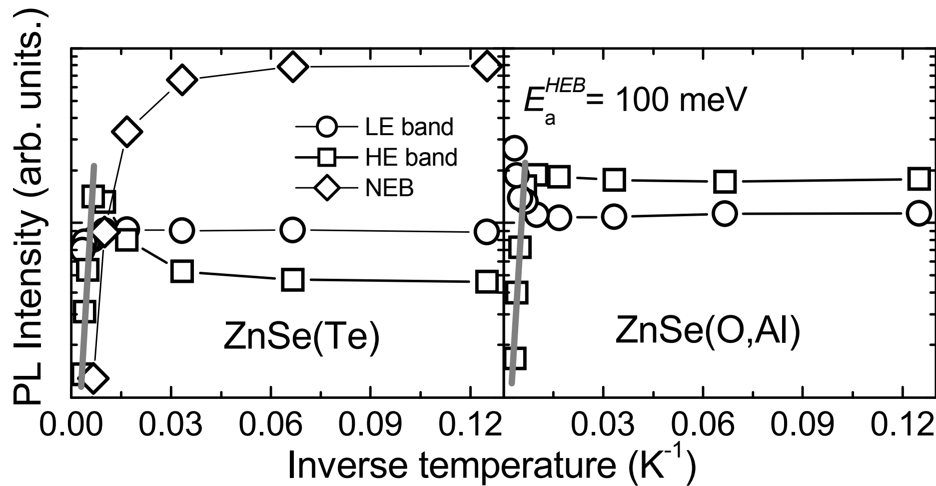

Fig. 3.2.2.3. The temperature dependence of emission intensity of LE (circles), HE (squares), and NBE (diamonds) PL bands measured in annealed ZnSe(Te) and ZnSe(O,Al) under pulsed two-step excitation. Solid grey line represents the Arrhenius dependence.

The intensity of LE band slightly decreases in ZnSe(Te) above ~150 K but experiences a significant increase by a factor of ~3 in ZnSe(O,Al) at room temperature.

Note that the dominating luminescence band in ZnSe(Te) is NBE emission, whose intensity exceeds that of the defect-related PL by a factor of 8 at 8 K.

3.3. Numerical simulation of temperature dependence of defect-related PL parameters

The increase in the LE band intensity at temperatures elevated up to the room temperature experimentally observed in annealed ZnSe(O,Al) is an unusual behavior but might be useful for applications of this crystal as scintillator material. This increase can be explained by thermal excitation of localized carriers and their subsequent capture by the radiative recombination centers responsible for the LE band. To prove this assumption, a simple model comprising one trapping and one recombination center without going into details on the recombination origin at this center was studied. The recombination model is illustrated in Fig. 3.3.1.

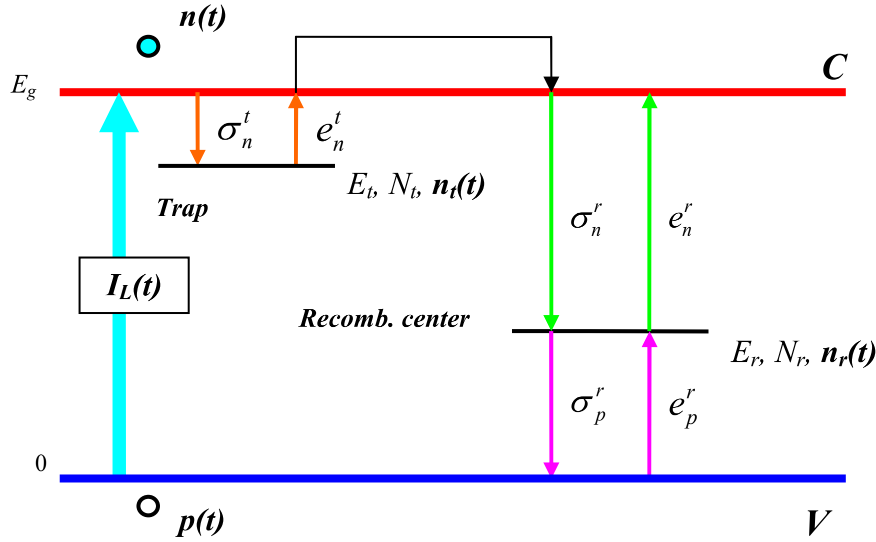

Fig. 3.3.1. Carrier recombination model for one trapping and one recombination centers.

A set of four coupled rate equations (3.3.1)-(3.3.4) was solved for the densities of free electrons $n(t,T)$, free holes $p(t,T)$, trapped electrons $n_t(t,T)$, and electrons captured by recombination centers $n_r(t,T)$, as in Ref [44]

$$\frac{dn}{dt} = G_L(t) - \sigma_n^t v_{th}^n n(N_t - n_t) + e_n^t n_t - \sigma_n^r v_{th}^n n(N_r - n_r) - e_n^r n_r \qquad (3.3.1)$$

$$\frac{dn_t}{dt} = \sigma_n^t v_{th}^n n(N_t - n_t) - e_n^t n_t \qquad (3.3.2)$$

$$\frac{dn_r}{dt} = \sigma_n^r v_{th}^n n(N_r - n_r) - e_p^r n_r - \sigma_p^r v_{th}^p p n_r + e_p^r (N_r - n_r) \qquad (3.3.3)$$

$$p = n + n_r + n_t - N_t \qquad (3.3.4)$$

Here, $G_L(t)$ denotes the free carrier generation rate (with Gaussian shape), N_t, N_r are the concentrations trapping and recombination centers, respectively. The density of the free holes p (eq. (3.3.4)) is evaluated using the carrier neutrality equation: $n + N_r^- = p + N_t^+$, where $N_t^+ = N_t - n_t$ and $N_r^- = n_r$. The cross-sections σ_n^t, σ_n^r (σ_p^r) of electron (hole) capture to electron traps and recombination centers, respectively, were assumed to depend on temperature as $T^{1/2}$ [45]. The thermal velocities of electrons and holes, v_{th}^n and v_{th}^p, respectively, are proportional to $T^{1/2}$. Thermal ionization rates e_n^t, e_n^r, and e_p^r describe the ionization of electrons from traps and recombination centers and holes from recombination centers, respectively. They are related to the capture cross sections by the following expressions:

$$e_n^t = \sigma_n^t v_{th}^n N_c \exp(-\frac{E_t}{kT}),\; e_n^r = \sigma_n^r v_{th}^n N_c \exp(-\frac{E_r}{kT}),\; e_p^r = \sigma_p^r v_{th}^p N_v \exp(-\frac{E_g - E_r}{kT}). \qquad (3.3.5)$$

Here, N_c and N_v denote the effective densities of states in the conduction and valence band, respectively, $N_{c(v)} = 2(m_{c(v)}^* kT / 2\pi\hbar^2)^{3/2}$, and k is the Boltzmann constant. For simplicity, a temperature-independent bandgap value E_g= 2.73 eV was used for the entire temperature range. E_t and E_r are the depths of the trap and recombination centers. The values of 0.145m_0 and 0.75m_0 were used for the effective masses of electron m_e^* and

hole m_h^*, respectively. We used the values for the recombination center parameters as in Ref. [46]: E_r = 700 meV, σ_n^r = 2×10^{-20} cm^2, σ_p^r = 10^{-16} cm^2, and N_r = 10^{17} cm^{-3}. The capture cross-section for the Coulombic attractive trapping center was fixed at the value of σ_n^t = 10^{-15} cm^2 [47, 17]. The trap density N_t was a free parameter (the best fit value is 2.7×10^{18} cm^{-3}), while the calculations have been carried out for several trap depths E_t in the range from 26 meV (corresponding to the hydrogen-like donor in ZnSe) to 150 meV. Initial conditions at t_0 = 0 were $n(0) = 0$, $n_t(0) = 0$, and $n_r(0,) = N_r$, i.e., all trapping centers were assume to be ionized and recombination centers to be occupied with electrons.

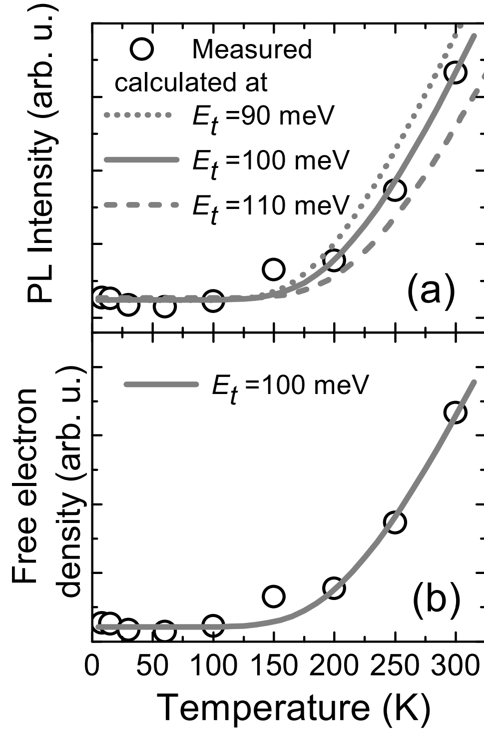

Fig. 3.3.2. The temperature dependence of PL intensity calculated according to equation (5) for trap activation energies of 90, 100, and 110 meV (lines in a) and of free electron density (solid line in b). The experimental dependence of PL intensity on temperature in ZnSe(O,Al) crystal is depicted by dots.

The temperature dependence of the carrier densities were obtained by solving the

set of equations (3.3.1) –(3.3.4) at fixed temperatures and calculating the densities at a fixed time $t_f = 2\Delta$ after the laser pulse peak, where Δ is the laser pulse duration.

According to equation (4), PL intensity was calculated as

$$I_{PL}= \sigma_p^r \, v_{th}^p \, n_r(t_f,T) p(t_f,T) \, . \qquad (3.3.6)$$

The temperature dependence of the PL intensity at different trap level depths is presented by the solid lines in Fig. 3.3.2. (a). The thermal ionization of traps at elevated temperatures results in an enhancement of the PL intensity. The best fit of the calculated and measured results was obtained at the trap ionization energy of 100 meV.

The free electron density calculated according to the equation set (3.3.1) –(3.3.4) is plotted as a function of temperature in Fig. 3.3.2. (b). The increase in the electron density with increasing temperature proceeds at the trap ionization energy of 100 meV at the same rate as the increase in PL intensity. This is an indication that the electrons thermally ionized from the trap centers are responsible for the enhancement of the LE band.

It is worth noting, that the energy barrier for quenching of the HE band is 100 meV, i.e., coincides with the ionization energy (100 meV) of the traps that are feeding, as discussed above, the centers responsible for the LE band. This coincidence implies that a considerable part of the electrons thermally ionized from the donor states involved in the recombination resulting in the HE band are captured by the donors in the centers responsible for LE band. A similar enhancement of the HE band at the expense of the LE band probably occurs also in the ZnSe scintillators doped with Te (see Fig. 3.2.2.3. (a)). However, this effect is not so strong as in ZnSe(O,Al) due to a lower density of the centers responsible for the HE band, as discussed above. Note that the HE band also experiences a temperature-induced enhancement. This enhancement is more pronounced

in annealed ZnSe(Te) than in ZnSe(O,Al), starts at lower temperature than the enhancement of the LE band and becomes overwhelmed due to quenching at elevated temperatures. The HE band enhancement is probably caused by thermal ionization of shallow donors.

3.4 The TRPL spectroscopy of defect-related luminescence

The PL peaks position of the two defect-related PL band in the crystals under study depends on the delay time. This behavior may be attributed to the carriers recombination in DAPs. To distinguish the contribution of the stable LE PL band, PL experiments were carried out at low temperature (8 K). The PL spectra at delays of 0, 1, and 10 μs after the excitation pulse are shown for annealed ZnSe(O,Al) and ZnSe(Te) in Fig. 3.4.1 (a) and (b), respectively. The emission on the high-energy end of the spectrum measured in ZnSe(Te) at zero delay is caused by near-band-edge emission. The two defect-related bands in the both samples were fitted with the two Gaussian curves. The best fits for the bands and the entire spectrum are depicted in Fig. 3.4.1. by green and red lines, respectively. Vertical lines indicate the peak position of LE band at zero delay.

As expected for DAP recombination, the increase of the delay time results in a red shift of the emission band due to Coulomb interaction in DAPs [48,49]. The photon energy depends on the mean distance between donor and acceptor $<r>$ as

$$h\nu\left(<r>\right)=E_g-\left(E_a+E_d\right)+\frac{e^2}{\varepsilon_r<r>} \tag{3.4.1}$$

Here, E_d and E_a are energies of isolated donor and acceptor, respectively; $<r>=\left(3/(4\pi N_{DAP})\right)^{1/3}$, where N_{DAP} is the density of occupied DAP. Thus, the Coulomb interaction term in (3.4.1) can be expressed through N_{DAP}.

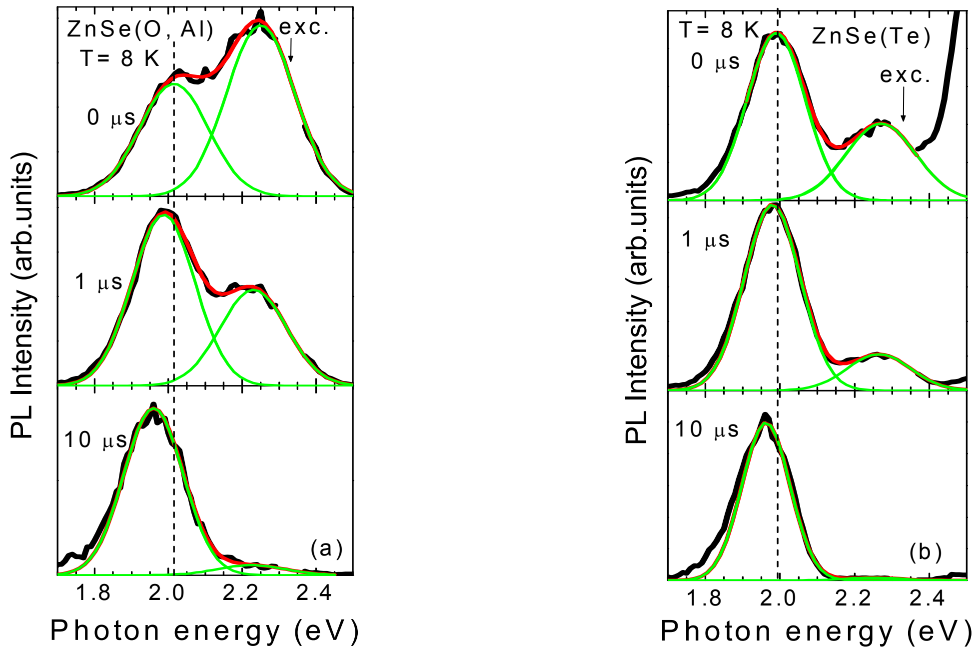

Fig. 3.4.1. PL spectra of ZnSe(O,Al) (a) and ZnSe(Te) (b) measured at 8 K temperature at different delays (indicated) after excitation pulse. The best fits for separate bands and entire spectrum are depicted by green and red lines, respectively.

During a pulsed excitation, the emission peak position depends on N_{DAP}, while the influence vanishes at long delays. Thus, the band shift enables estimation of N_{DAP}, i.e. the density of occupied DAP, which is the lower limit of the total density of DAP. Note, that the intensity of the LE band increases in the delay region from 0 to 1 μs and reaches the peak value at 1 μs. Thus, it is assumed that N_{DAP} also reaches its highest value at 1 μs after the laser excitation pulse.

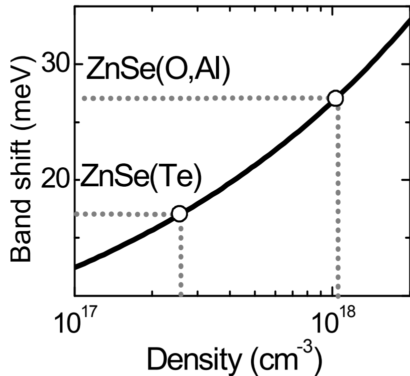

Fig. 3.4.2. Band shift due to Coulomb interaction in DAPs (solid line) as a function of density of occupied DAPs in ZnSe. Points indicate the shift values observed in annealed ZnSe(Te) and ZnSe(O,Al) samples.

The Coulomb interaction energy (the last term in Eq. (3.4.1)) as a function of the density of occupied DAPs, N_{DAP}, is depicted in Fig. 3.4.2.

The experimentally observed band redshifts of ~17 meV in ZnSe(Te) and ~27 meV in ZnSe(O,Al) correspond to the densities of 2.5×10^{17} cm^{-3} and 1×10^{18} cm^{-3}, respectively. These values are slightly smaller than the corresponding DAP densities extracted from PL decay measurements (see above). This underestimate is feasible, since the initial N_{DAP} in this experiment was lower than the total DAP density, and the delay of 10 μs used in this experiment does not correspond to the complete vanishing of the last term in (3.4.1). Moreover, for the closest DAPs, Van der Waals interaction between donor and acceptor should be taken into account, and a correction term due to the correlation interaction of electron and hole and an electrostatic correction term due to the overlap of the wave functions of donor and acceptor have to be included in Eq. (3.4.1) [49]. Despite all these accuracy limitations, both estimates based on PL decay kinetics and band shift show that the density of radiative DAPs in ZnSe(O,Al) is nearly by an order of magnitude higher than that in ZnSe(Te).

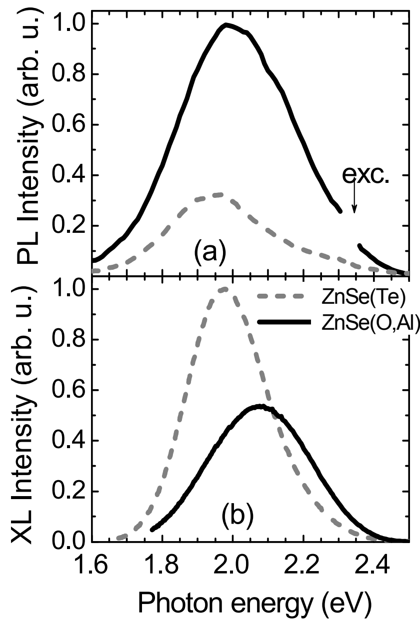

Fig. 3.4.3. Luminescence spectra measured in ZnSe(Te) (dashed curves) and ZnSe(O,Al) (solid curves) under two-step photoexcitation at 2.33 eV (indicated by an arrow) (a) and X-ray excitation (b) at room temperature.

The room temperature PL spectra of annealed ZnSe(Te) and ZnSe(O,Al) monocrystals are presented in Fig. 3.4.3. (a). Both samples were annealed under nominally identical conditions. The PL intensity in ZnSe(O,Al) was by a factor of ~3.3 higher than that in ZnSe(Te). However, this intensity enhancement was not observed in luminescence of these two samples under X-ray excitation (see Fig. 3.4.3. (b)). Instead, the XRL intensity of ZnSe(Te) was by a factor of ~1.6 higher than that of ZnSe(O,Al). This discrepancy between PL and XRL could be caused either by different internal emission efficiency or by different excitation conditions.

A rough estimation demonstrates that the density of optically-excited recombination centers in

this experiment may exceed that of the X-ray-excited by more than 10 orders of magnitude. Thus, the optical two-step excitation can saturate the channels of carrier radiative recombination in ZnSe(Te), while in ZnSe(O,Al) the saturation might not be occur. Thus, PL intensity of ZnSe(O,Al) will exceed that of ZnSe(Te) at high optical excitation levels.

3.5 Photoluminescence decay kinetics

The spectra of defect-related photoluminescence in the ZnSe crystals under study consist of two strongly overlapping bands. The HE band is strongly thermally quenched at room temperature, has a rapid decay of the order of ~0.7 µs, and has smaller importance for practical applications of ZnSe crystals as scintillator material. Thus, the further study here is focused mainly on the LE band. The decay of the LE band intensity measured at the peak positions, 1.94 eV in ZnSe(Te) and 1.95 eV in ZnSe(O,Al), at different temperatures in the range from 8 to 300 K is presented in Fig. 3.5.1. (a) and Fig. 3.5.1. (b), respectively.

At all temperatures, the decay is nonexponential. It is reasonable to assume that the band is a result of radiative DAP recombination. In this process, the decay rate depends on the distance between donor and acceptor in the corresponding pair. As a result, the PL decay rate at a fixed spectral position due to DAP recombination can be expressed as [48]:

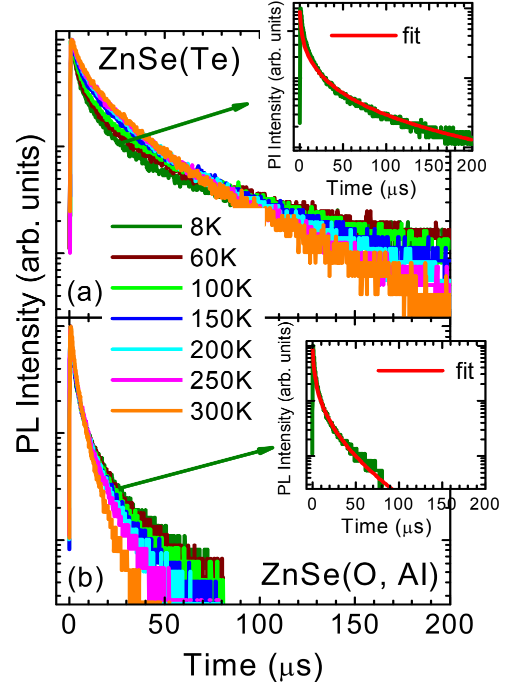

Fig. 3.5.1. Kinetics of PL low- energy band measured at different temperatures (indicated) in annealed ZnSe(Te) at 1.94 eV (a) and ZnSe(O,Al) at 1.95 eV (b) crystals. The best fits of the decays calculated using equation (1) with those measured at 8 K are presented in the insets.

$$I_E(t) = 4\pi N_d \left(\frac{e^2}{\varepsilon_r}\right)^3 \frac{1}{E^4} W_0 \times \left\{ \exp\left[-\frac{2e^2}{\varepsilon_r E a_B} - W_0 t \exp\left\{ -\frac{2e^2}{\varepsilon_r E a_B} \right\} \right] \right\} \times$$
$$\times \exp\left[4\pi N_d \int_0^\infty \left\{ \exp\left[-W(r)t \right] - 1 \right\} r^2 dr \right]. \qquad (3.5.1)$$

Here, $E = E_g - (E_A + E_D) - h\nu$ is the DAP Coulomb interaction energy at a fixed $h\nu$, $\varepsilon_r = 16\varepsilon_{opt}\varepsilon_{stat} / (11\varepsilon_{opt} + 5\varepsilon_{stat})$ is the effective dielectric constant in polar semiconductor [50], $\varepsilon_{opt} = 6.66$ [51], $\varepsilon_{stat} = 8.66$ [52] in ZnSe, thus is $\varepsilon_r = 7.92$, N_d is the concentration of the majority constituent of DAPs, $W(r) = W_0 \exp(-2r/a_B)$ is the DAP recombination rate, r is the distance between donor and acceptor, W_0 is the DAP recombination rate at the fixed spectral position and $r \to 0$, and a_B is the Bohr radius of the shallower impurity in the DAP (donor in ZnSe).

The fitting procedure has been carried out by varying W_0 and N_d as free parameters for the best fit in ZnSe(Te) sample (by limiting the upper range of W_0 at 2.7×10^9 s^{-1}). The Bohr radius and the DAP Coulomb interaction energy E were fixed. The value of DAP Coulomb interaction energy was estimated from experiment, as described in section 3.4.

The fitting parameters are listed in Table 3.5.1. It can be concluded, that the carrier recombination in ZnSe(O,Al) is faster because of the higher density of DAP and the faster recombination within DAP (i.e. a stronger overlap of donor and acceptor wave functions) than that in ZnSe(Te).

Table 3.5.1. Best parameters for fitting the experimental PL kinetics with calculations using DAP recombination model (eq. 3.5.1).

	ZnSe(Te)	ZnSe(O,Al)
W_0, s^{-1}	6×10^7	9×10^7
a_B, nm	1.5	1.3
N_d, cm^{-3}	2.4×10^{18}	4.7×10^{18}
E, meV	20	30

3.6 Simulation of photoluminescence excitation spectra of defect-related PL

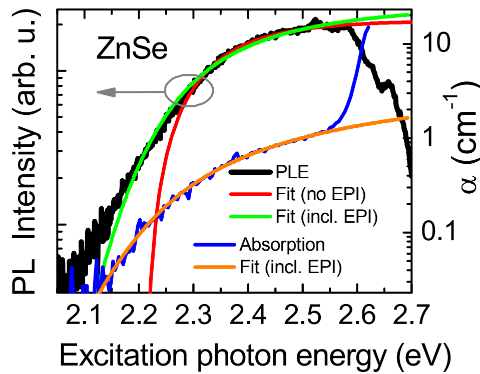

Fig. 3.6.1. Measured PLE (black curve) and absorption (blue curve) spectrum in undoped ZnSe, simulated PLE spectra without EPI (red curve) and including EPI (green curve), and simulated absorption spectrum (orange curve) using equation (3.6.1) and (3.6.2), T =295 K.

Photoluminescence excitation spectra of the annealed ZnSe(Te), ZnSe(O), ZnSe(O,Al) and undoped ZnSe crystals were recorded at room temperature at the fixed spectra position at ~1,94 eV (640 nm), ~1,97 eV (630 nm), ~2,07 eV (600 nm), and ~1,94 eV (640 nm), respectively. Fluorescence spectrometer *LUMINA* (*Thermo Fischer Scientific*) has been used to record the PLE spectra in the spectral range from 2 to 3.2 eV. The PLE spectrum of undoped ZnSe in the figure 3.6.1 is typical for all the crystals under study discussed in this section.

Intensity of LE PL band increases by increasing energy of excitation photon in the range from 2 to 2.6 eV. This behavior may be associated with dependence of absorption efficiency on the absorbed light wavelength. However, at the excitation photon energies above the band-gap the defect-related PL intensity drastically decreases due to nonradiative recombination at the crystals surface. Intensity of absorbed light can be expressed as $I_a(T,\hbar\omega) = I_0(1-\exp[-d\sigma(T,\hbar\omega)N])$, were d is the thickness of the sample, $\sigma(T,\hbar\omega)$ is the photoionization cross-section, which depends on temperature T and photon energy $\hbar\omega$, N is the density of impurities, and I_0 is the excitation light intensity. Thus, intensity of absorbed light is related to the PL intensity as

$$I_{PL}(T,\hbar\omega) = QY \times I_0(1-\exp[-d\sigma(T,\hbar\omega)N]). \quad (3.6.1)$$

Here QY is the PL quantum yield. In Eq. (3.6.1) it is assumed, that QY is constant and doesn't depends on the excitation photon energy. Thus, the photoionization cross-section determines dependence of PL efficiency on the excitation photon energy. At low temperatures photoionization is well described by the Lucovsky delta-potential model [53]. However, the Lucovsky model ignores electron-phonon interaction, which may significantly influence cross-section at elevated temperatures. The theoretical dependence of photoionization cross-section $\sigma(T,\hbar\omega)$ including a local electron-phonon interaction under preserved Lucovsky delta-potential model approach for the forbidden transition has the following form [54,55,56]

$$\sigma(\hbar\omega,T) = \frac{\sigma_0}{\hbar\omega\sqrt{\pi\Theta}} \int_1^\infty \frac{(t-1)^{3/2}}{t^2} \exp[-\frac{(t-\hbar\omega/E_i)^2}{\Theta}]dt. \quad (3.6.2)$$

Here σ_0 is a coefficient which is independent on temperature and has weak dependence on the excitation photon energy, E_i is the photoionization threshold energy, t is the dimensionless integration parameter, $\Theta = (a_{EPI}\hbar\Omega/E_i)^2(\coth(\hbar\Omega/2kT)-1)$ is the temperature-dependent parameter that determines smoothing of photoionization spectra due to electron-phonon interaction, a_{EPI} is the dimensionless constant of electron-phonon coupling, and T is temperature.

The equations (3.6.1) and (3.6.2) were solved numerically to perform simulation of the PLE spectra. The delta-potential model for cross-section spectrum (as described in [53]) has been also applied to evaluate of an influence of the EPI on the photoionization threshold energy (red and green curves in Fig. 3.6.1).

The sample thickness d =0.1 cm, PLE amplitude $QY \times I_0 = A$, and the local phonon energy $\hbar\Omega$ (see the table 3.2.2.1) were set as the fixed simulation parameters. The constant a_{EPI} was bound to photoionization threshold and PL peak using relation $E_i = E_{PL} + a_{EPI}^2\hbar\Omega$, where $a_{EPI}^2\hbar\Omega$ is the Stokes shift [56], and E_{PL} is PL peak corresponding to "e-A" transition, which was fixed at E_{PL} = 1.907 eV for ZnSe(Te), ZnSe(O), and ZnSe and E_{PL} = 1.923 eV for ZnSe(O,Al) (see Fig. 4.2.2.1). The photoionization threshold E_i and the factor $\alpha_0 = \sigma_0 \times N$ were varied as free parameters to get the best fit. The optical absorption spectra are also well described by equation (3.6.2) and has been simulated for annealed ZnSe and ZnSe(O) crystals by varying a_{EPI}, E_i and factor α_0 as the free simulation parameters (see orange curve in Fig. 3.6.1). The simulation parameters ensured the best fits are listed in the table 3.6.1.

The values of the evaluated E_i and a_{EPI} constants are ~ 2.16 eV and 3.3, respectively, for ZnSe(Te), ZnSe(O), and ZnSe crystals. While a_{EPI} in ZnSe(O,Al) is higher than that in the other crystals, and indicates on the stronger EPI. Energy relaxation of an recombination center through the Franck-Condon process can be evaluated as $\Delta_{FC} = a_{EPI}^2\hbar\Omega/2$ [56], and an acceptor energy level above VBM is $E_m = E_g - (E_{PL} + \Delta_{FC})$, where E_g =2,7 eV is the band gap of ZnSe at the room temperature.

Finally, summarizing this section, it can be concluded that the acceptor level energy E_M and an EPI constant a_{EPI} is 0.67 eV and 3.3, respectively, in ZnSe(Te), ZnSe(O) and ZnSe crystals, and well agrees with that estimated for ZnSe(Te) in [13] (E_M = 0.67 eV, a_{EPI} = 3.2 eV). Whereas doping of ZnSe with oxygen by adding aluminum oxide into the

melt reduces energy of acceptor level to $E_M \approx 0{,}5$ eV and enhances strength of EPI compared to that in the other under study.

Table 3.6.1 Parameters, estimated from the simulation of the PLE spectra of LE PL band and absorption spectra: photoionization threshold E_i, peak of LE PL band E_{PL}, Franck-Condon energy shift Δ_{FC}, dimensionless EPI constant a_{EPI}, local phonon energy $\hbar\Omega$, and acceptor level E_M.

	ZnSe(Te)	ZnSe	ZnSe(O)	ZnSe(O,Al)
E_{PL}, eV	1.907	1.907	1.907	1.923
E_i, eV (Lucovsky model)	2.17	2.21	2.13	2.37
E_i, eV (eq. 3.6.2)	2.158	2.179	2.144	2.470
E_i, eV (from absorption)	--	2,183	2.154	--
Δ_{FC}, eV	0.125	0.133	0.118	0.273
a_{EPI} (from PLE)	3.3	3.3	3.3	5.2
a_{EPI} (from absorption sp..)	--	4.1	4.1	--
$\hbar\Omega$, eV	0.0237	0.0244	0.0216	0.0202
E_M, eV	0.668	0.660	0.675	0.504

Chapter 4. Defect-related photoluminescence in ZnSe scintillation crystals codoped with rare earth oxides

4.1. The influence of codoping by rare earth oxides on defect-related luminescence

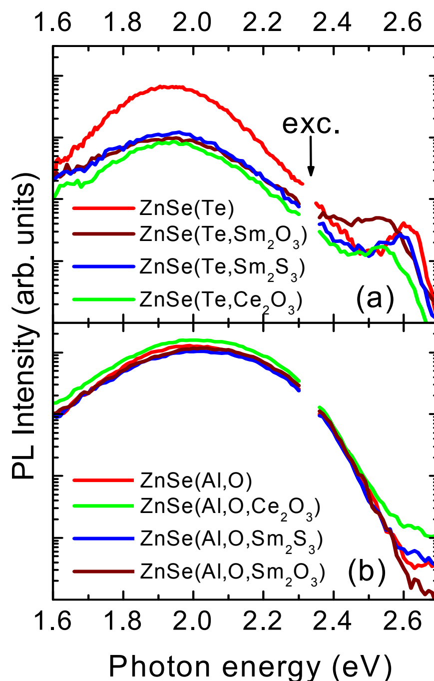

Fig. 4.1.1. Defect-related PL spectra of ZnSe crystals doped with tellurium (a) and oxygen and aluminum (b) and codoped with rare earth compounds (indicated).

The Figure 4.1.1 shows the PL spectra in ZnSe doped with tellurium (Fig. 4.1.1(a)) and aluminum oxide (Fig. 4.1.1(b)) and codoped with rare earth oxides. The two-step excitation at 2.33 eV was used for bulk excitation of the samples to avoid nonradiative recombination at the crystal surface. The photoluminescence signal was recorded at 1 µs delay after the excitation pulse. As can be observed, the codoping of conventional ZnSe(Te) scintillator with any RE compound results in a lower luminescence intensity. Meanwhile, codoping of ZnSe(O,Al) scintillator has no effect on its luminescence intensity. The observed influence of RE elements on photoluminescence is in consistence with the corresponding influence on X-ray luminescence revealed in the earlier study [57].

The codoping with RE compounds might also have influence on the shape of PL bands. The normalized spectra of codoped ZnSe(Te), ZnSe(O,Al), and ZnSe are presented in Fig. 4.1.2. All the spectra were measured under $h\nu_{exc}$ =3.81 eV excitation. The PL spectra in the codoped ZnSe(Te)

are broader than those in the crystals without RE doping. Note, however, that codoping of ZnSe(O,Al) scintillator has no effect on its PL spectrum. Thus, the additional selective excitation by monochromated halogen lamp light ($h\nu_{exc}$ =2.25 eV) of ZnSe(O,Al) luminescence (black line Fig. 4.1.2(b)) was implemented to perform the spectra decomposition procedure into separate luminescence bands, which is discussed here below.

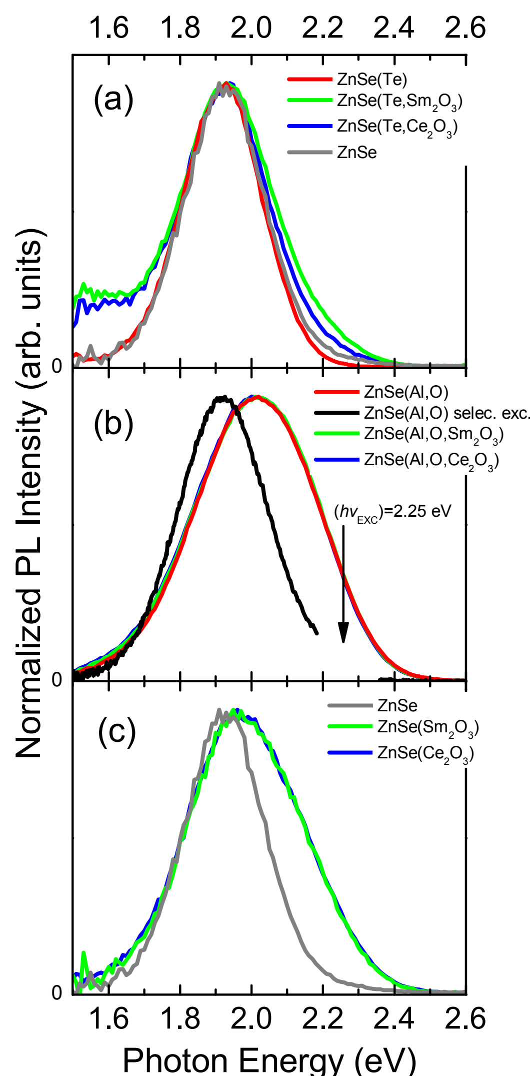

Fig. 4.1.2. Normalized spectra of defect-related PL band measured in ZnSe(Te) (a), ZnSe(O,Al) (b), and ZnSe (c) crystals codoped with rare earth oxides (indicated).

To study the nature of the spectral changes in photoluminescence of codoped ZnSe(Te) scintillators, the deconvolution of the spectra was performed using Alentsev-Fok deconvolution procedure as described in subsection 3.1.1. The deconvolution has been performed for all codoped samples under study: ZnSe(Te), ZnSe(O,Al), and ZnSe.

The deconvolution procedures in ZnSe(Te) and ZnSe were accomplished by comparing the PL in samples with and without RE doping, i.e. ZnSe(Te+RE) has been compared with ZnSe(Te), etc. The deconvolution of spectra in codoped ZnSe(O,Al) is more complicated, since codoping has no influence on PL spectrum. To accomplish the deconvolution procedure, it the PL spectrum of ZnSe(O,Al) crystal measured under selective excitation was used. The spectrum under selective excitation is peaked at 1.92 eV, instead of 2.01 eV under band-to-band excitation. Application of the Alentsev-Fok procedure to these pairs of the spectra measured under selective and band-to-band excitation enabled the deconvolution of PL spectra.

The spectra of all crystals consist of strongly overlapping HE, LE and infrared PL bands, peaked at 2.11, 1.92, and below 1.7 eV, respectively. The LE band dominates over other PL bands in ZnSe(Te) crystals without RE doping, while its fractional intensity in the codoped ZnSe(Te) crystals is in the range from 74% to 80%. The fractional intensity of the LE band is lower (down to 56 %) in ZnSe(O,Al) samples. The infrared PL band peaked approximately at 1.55 eV is significant only in the codoped ZnSe(Te) crystals, where its fractional intensity (~10 %) equals that of the HE band.

After doping with RE oxides, the spectra of ZnSe become similar to the spectra of ZnSe(O,Al) (see Fig. 4.1.2(c)). The spectrum consists of HE and LE PL bands with the fractional intensities of 34% and 66%, respectively. Since all of the RE compounds used for codoping contains oxygen, the similarity of the PL spectra is an indication that the

HE band appears in the samples containing oxygen. Therefore, it might be caused by optical transitions involving oxygen-related deep levels

4.2 The oxygen role in the codoped crystals

4.2.1 Absolute quantum yield of defect-related PL in the isoelectronically doped ZnSe crystals

To get a deeper insight into the influence of oxygen on the luminescence efficiency and spectrum of ZnSe-based scintillators the absolute quantum yield dependence on excitation photon energy and the selectively excited PL spectra in ZnSe single crystals doped with isoelectronic oxygen and tellurium was studied. The dependence of the absolute QY on excitation photon energy in ZnSe(Te), ZnSe(O), and ZnSe(O,Al) is presented in Fig. 4.2.1.1.

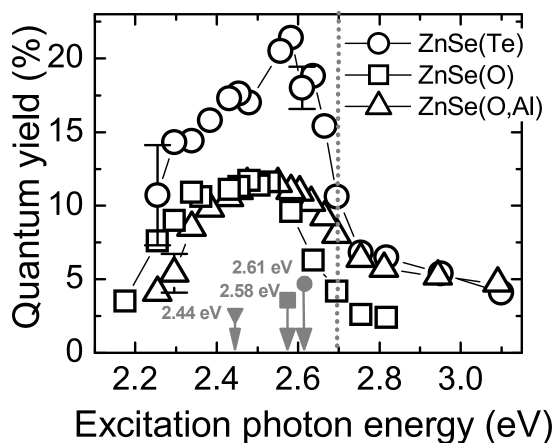

Fig. 4.2.1.1 Dependence of quantum yield of defect-related PL in ZnSe(Te) (circles), ZnSe(O) (squares), ZnSe(O,Al) (triangles) on excitation photon energy at room temperature. The arrows indicate the corresponding room temperature optical band gaps, grey doted line indicates the band gap in pure ZnSe at room temperature.

The dependence of QY on excitation photon energy has two distinct regions. The QY decrease at low excitation photon energy side is caused, apparently, by reabsorption of the luminescence as the absorption length increases. The decrease proceeds faster for ZnSe(O,Al). This feature might be caused either by stronger background absorption below the band gap or by a red shift of the absorption edge. The strong red shift (170 meV) of the absorption edge measured in ZnSe(O,Al) in respect to the edge measured in ZnSe(O) (see arrows in Fig. 4.2.1.1) implies that the shift is mainly responsible for the faster QY decrease at lower excitation photon energies observed in ZnSe(O,Al).

The highest QY of ZnSe(Te), 21 %, exceeds that in ZnSe(O) and ZnSe(O,Al) by a factor of ~1.9. The lower QY of the defect-related luminescence in the oxygen-doped ZnSe crystals indicates stronger nonradiative recombination in the crystal bulk compared to that in the conventional ZnSe(Te) scintillator. The lower QY of defect-related PL in ZnSe(O) and ZnSe(O,Al) also might be associated with chemical and physical properties of isoelectronic O_{Se} atoms having a smaller ionic/covalent radii and higher electronegativity than that of the substituted Se atom [58,59,60,61,62]. Note, that ZnSe(O) and ZnSe(O,Al) exhibit similar QYs (~12 %), though oxygen was introduced into these crystals using different techniques.

The decrease in QY above the band gap is caused by nonradiative recombination at the crystal surface as the absorption depth for the excitation photons becomes small. An effective thickness of the damaged surface layer can be evaluated as follows.

The QY in the crystals under study decreases when excitation photon energy exceeds ~2.58 eV and stabilizes (become constant) above 2.75 eV. At increasing

excitation photon energy, the effective absorption depth decreases (more photons are absorbed in surface layer). The total number of emitted photons in the bulk and the surface layer can be expressed as the sum $N_E = N_{Es} + N_{Eb} = QY_s N_{Ap} + QY_b N_{At}$, and the number of absorbed photons is $N_A = N_{As} + N_{Ab}$. Hereafter, the subscripts s and b denotes "**s**urface" and "**b**ulk" layer, respectively. The effective absorption depth in annealed ZnSe(Te) for 2.58 eV and 2.75 eV photons is ~20 cm^{-1} (see Fig.3.1.2.1) and 4×10^4 cm^{-1} [63], respectively. The corresponding effective absorption depths are 500 μm and 0.25 μm. Schematic structure of the structure of the samples under study is demonstrated in Fig.4.2.1.2. Thus, the total quantum yield of the "layered" crystal can be expressed as

$$QY = \frac{QY_s N_{As} + QY_b N_{Ab}}{N_{As} + N_{Ab}} = \frac{QY_s}{1 + N_{Ab} / N_{As}} + \frac{QY_b}{1 + N_{As} / N_{Ab}} \quad (4.2.1.1)$$

Here, the photon number absorbed in the surface and bulk layers are $N_{As} = N_o(1-\exp[-\alpha d_s])$ and $N_{Ab} = N_o\exp[-\alpha d_s](1-\exp[-\alpha d_b])$, where N_o is the number of photons entering the crystal. , α is the absorption coefficient, and d_s ir d_b are thicknesses of surface and bulk layers, respectively. Thus, after some mathematical transformation, the total QY is

$$QY = \frac{QY_s}{1 + \dfrac{1 - \exp[-\alpha d_b]}{\exp[\alpha d_s] - 1}} + \frac{QY_b}{1 + \dfrac{\exp[\alpha d_s] - 1}{1 - \exp[-\alpha d_b]}} \quad (4.2.1.2)$$

As follows from Eq.(4.2.1.2), when $\alpha d_b >> \alpha d_s$, then $QY \rightarrow QY_b$, and, vice versa, when $\alpha d_b << \alpha d_s$, then $QY \rightarrow QY_s$. Thus, the decrease of the QY below the band gap might be explained by the presence of a thin surface layer with strong nonradiative recombination.

The simulated dependence of QY on the effective absorption depth (d_{eff}=1/α) (Eq. 4.2.1.2) is shown in Fig. 4.2.1.2 by solid blue curve. The values of optical absorption coefficients were taken from Fig. 3.1.2.1 for ZnSe(Te) below 2.58 eV and from [63] for the region above 2.58 eV. The measured QY as function of effective absorption depth for annealed ZnSe(Te) samples (thickness of 0.5 and 2 mm) is shown in Fig. 3.1.2.1. The fitting was employed at fixed parameters: QY_b = 22.5 %, QY_s = 3.5 %, ant the sample thickness d_b = 500 or 2000 μm. Only the thickness d_t of the surface layer was varied as a free parameter. The best fit was ensured by d_t = 230 μm. The simulation results were compared with the measurements of spatially-resolved luminescence on the crystals surface.

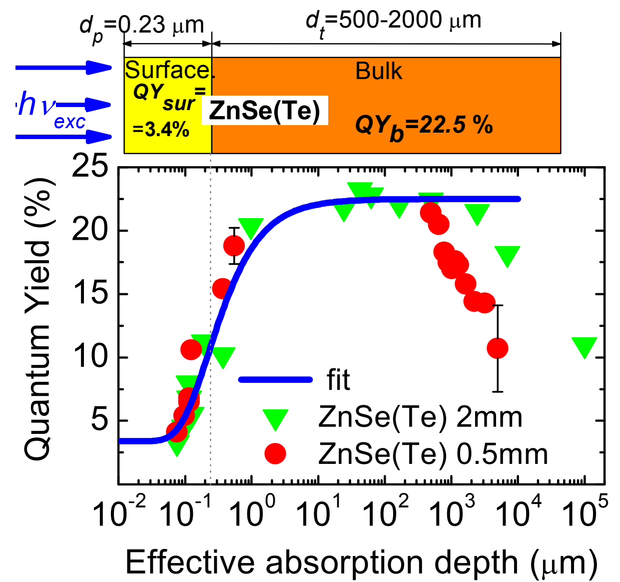

Fig. 4.2.1.2. Dependence of quantum yield on effective absorption depth of defect-related PL in ZnSe(Te) at the sample thickness of 0.5 mm (circles) and 2 mm (triangles). The blue solid curve corresponds to simulated dependence.

The photoluminescence intensity mapping of annealed ZnSe(O,Al) recorded using a confocal microscope is sown in Fig. 4.2.1.3. The confocal microscopy revealed inhomogeneity in spatial distribution of PL intensity on the scale of hundreds of nanometers. The observed inhomogeneity seemingly arises from chemical contamination

and mechanical polishing of the crystal surface. The intensities of the both defect-related and NBE PL bands decrease by more than an order of magnitude in the vicinity of the damaged areas.

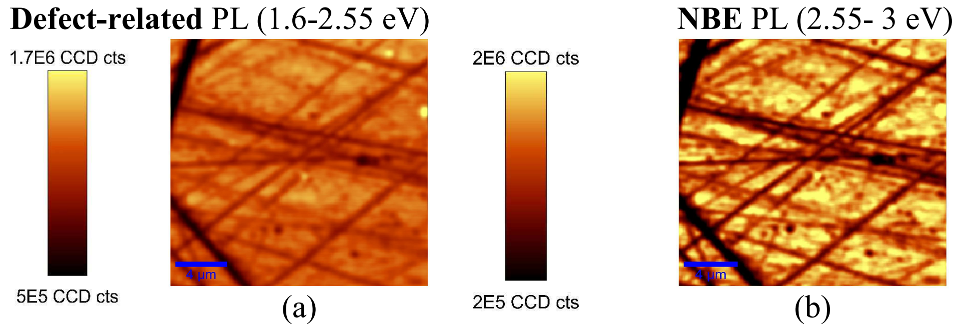

Fig. 4.2.1.3. Spectrally integrated intensity mapping (20x20 µm) of defect-related (a) and NBE (b) PL of annealed ZnSe(O,Al) crystal at $h\nu_{exc}$ = 3.06 eV and excitation power density of 715 kW/cm^2.

4.2.2 Defect-related PL spectra of tellurium and oxygen doped ZnSe crystals under excitation at different photon energy

The spectra of defect-related PL in ZnSe(Te), ZnSe(O), and ZnSe(O,Al) under excitation at different photon energies are presented in Fig. 4.2.2.1. All the spectra in Fig. 4.2.2.1 are normalized for the convenient comparison of the band shapes.

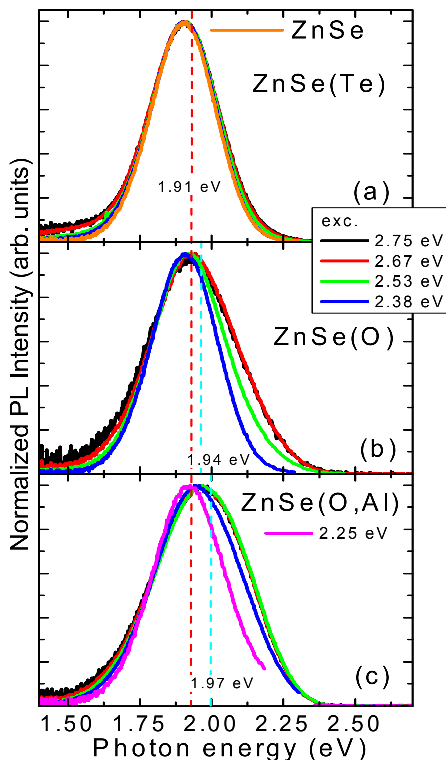

Fig. 4.2.2.1. Spectra of defect-related PL in ZnSe(Te) (a), ZnSe(O) (b), and ZnSe(O,Al) (c) under excitation with different photon energy (indicated). The spectrum of ZnSe under interband excitation (orange curve in Fig. 4.2.2.1a)) is presented for reference

The PL bands of ZnSe(Te) and ZnSe are peaked at 1.91 eV, and their band shapes exhibit no significant dependence on excitation photon energy. These spectra can be well fitted by a single Gaussian function. Meanwhile, the PL bands of ZnSe(O) and ZnSe(O,Al) change their shapes and shift to the low energy side by 30 and 60 meV, respectively, as the excitation photon energy is decreased from the band-to-band excitation down to 2.25 eV. The dependence of the spectral shapes on excitation photon energy indicates a complex nature of the defect-related PL spectrum in the oxygen-containing ZnSe crystals.

The Alentsev-Fok deconvolution procedure of ZnSe(O) and ZnSe(O,Al) PL spectra was accomplished by processing the spectra measured under band-to-band excitation and excitation at $h\nu_{exc}$ < 2.3 eV when the LE band becomes dominant. The spectra of both ZnSe(O) and ZnSe(O,Al) are complex and consist of infrared, LE, and HE PL bands peaked at 1.70 eV, 1.91 eV and 2.09 eV, respectively.

The composition of the PL spectra in ZnSe(O) and ZnSe(O,Al) is similar to that in ZnSe codoped with RE oxides. Since codoping with rare earths does not change the PL spectrum, the spectral changes imposed by codoping with RE oxides has the same result as the direct doping by oxygen.

Note, that the position of the HE band strongly depends on excitation power density. At the low excitation power density, the peak of the HE band shifts from 2.09 to 2.11, to 2.29 eV, as the excitation power density is increased in a wide range from 1 μW/cm^2 to 1.5 W/cm^2, to 484 kW/cm^2, respectively. At high excitation power densities, a higher DAP density is excited, and the mean distance in the DAP is reduced. Thus, the excitation-induced blueshift of the HE band can be explained by enhancement of Coulomb interaction as the donor-acceptor distance decreases at elevated excitation intensities.

4.3. PL decay in the codoped ZnSe crystals under intense photoexcitation

The study of luminescence decay kinetics has been performed in codoped ZnSe scintillation crystals. Room temperature photoluminescence spectra measured in the conventional ZnSe(Te) scintillator at different delays after the excitation pulse are presented in Fig. 4.2.3.1. The PL spectra consist of two strongly overlapping bands: the LE band peaked at 1.91 eV and the HE band peaked at 2.16 eV. Both the PL bands were observed in the spectra of all the crystals under study. As clearly seen in Fig. 4.2.3.1, HE band decays considerably faster than the LE band does. The study is mainly focused on the LE PL band. It was observed that the spectrum of ZnSe(Te,Sm_2O_3) contains an additional PL band peaked at 1.51 eV(820 nm) (Fig. 4.2.3.2), which has not been observed in any other sample under study. A band with a similar spectral position was previously observed in ZnSe/MoO_3 bilayer, however, its origin was unrevealed there [64]. On the other hand, the PL emission peak at 1.51 eV agrees well with the indirect band gap in ZnO-ZnSe heterostructure [65]. Thus, the 1.51 eV band might be related to defects involving oxygen or ZnO clusters in the host ZnSe lattice [29].

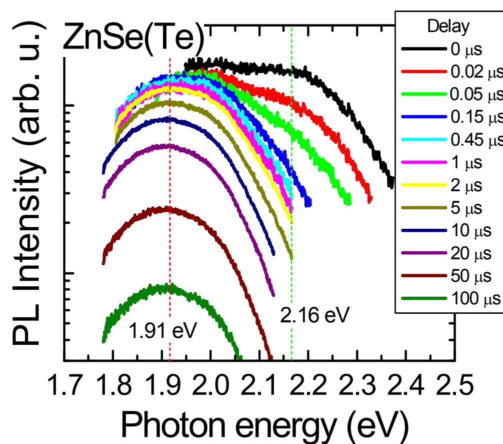

Fig. 4.2.3.1. PL spectra of ZnSe(Te) scintillation crystals at different delays (indicated) after pulsed excitation at $h\nu_{exc}$ =2.58 eV.

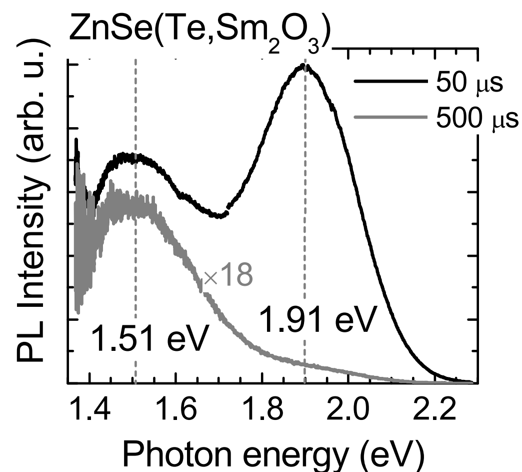

Fig. 4.2.3.2. PL spectra measured at 50 μs (black curve) and 500 μs (grey curve) delays after pulsed excitation in ZnSe(Te,Sm_2O_3). Multiplication factor is indicated.

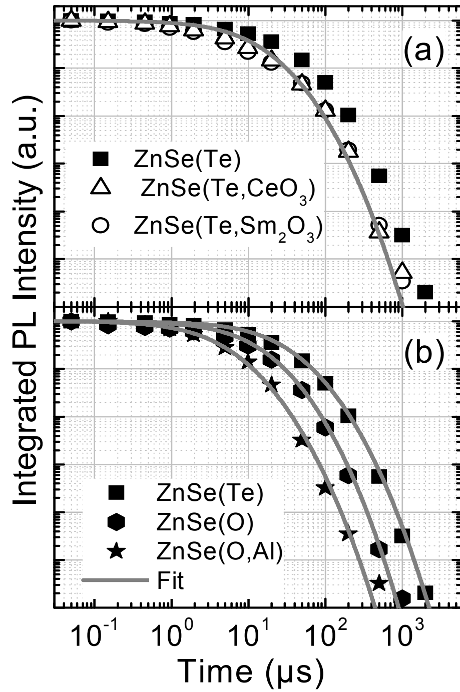

Fig. 4.2.3.3. Spectrally integrated and normalized PL decay kinetics measured in isoelectronically doped ZnSe additionally codoped with rare earth oxides (indicated). Solid curves correspond to calculated kinetics of decay via donor-acceptor pair recombination.

The decay kinetics of the spectrally integrated PL in ZnSe doped with isoelectronic Te, O and codoped with rare earth oxides are presented in Fig. 4.2.3.3. Codoping of conventional ZnSe(Te) crystal with RE oxides increases the carrier radiative recombination rate (Fig. 4.2.3.3(a)). The photoluminescence decay rate in ZnSe(O) exceeds that in the conventional ZnSe(Te). The highest radiative recombination rate was observed in ZnSe codoped with oxygen and aluminum (Fig. 4.2.3.3(b)).

The photoluminescence decay in all the samples under study is nonexponential and can be attributed to carrier radiative recombination in DAP. The measured PL kinetics were fitted using expression for spectrally-integrated DAP kinetic, which is similar to equation (3.5.1), and detailed is described in [48].

The recombination rate W_0 and the donor density N_d were varied as independent parameters to get the best fit. The value of the actual Bohr radius a_B was set taking into account the thermal ionization energy (see Table 3.2.1.1): 1.5 nm for ZnSe(Te+RE), 1.5 nm for ZnSe(O), and 1.3 nm for ZnSe(O,Al).

The fit parameters N_d and W_0 for the samples under study are listed in Table 4.3.1.

Table 4.3.1. Fit parameters for description of DAP PL kinetics.

	ZnSe(Te)	ZnSe(Te+RE)	ZnSe(O)	ZnSe(O,Al)
N_d ×$\mathbf{10^{19}}$ (cm^{-3})		1.9		3
W_0×$\mathbf{10^5}$ (s^{-1})	2	4.3	4.3	10

Frequency-domain measurements

The results obtained by studying the PL decay kinetics in time domain were supported by the measurements in frequency domain. ZnSe-based scintillators usually operate at low excitation levels, thus, it is important to characterize the scintillator performance at excitation levels close to the real excitation conditions. To ensure the low excitation level, blue LED was used as excitation source and the emission decay kinetics was studied using the frequency domain luminescence lifetime measurement technique. The modulation frequency dependences of the phase shift between harmonically modulated LED excitation light and PL response in ZnSe(Te), ZnSe(O), and ZnSe(O,Al) are presented in Fig.4.2.3.3. To fit the measured phase shift curves, Fourier transformation for the DAP luminescence decay was applied. A good agreement of the measured and calculated curves was achieved. In fitting the Fourier-transformed function with experimentally obtained dependences, the same values of the fit parameters W_0, N_d,

and a_B were used as for the fitting of the PL decay obtained in the time domain PL (see Table 4.3.1).

The faster PL decay in ZnSe(O) and ZnSe(Te+RE) can be explained by a higher DAP recombination rate W_0 compared to that in ZnSe(Te). Meanwhile, the donor density and the radiative recombination rate in ZnSe(O,Al) exceed those in ZnSe(Te), ZnSe(Te+RE), and ZnSe(O). Meanwhile, the X-ray luminescence intensity of ZnSe(O,Al) crystals is lower by a factor of 1.6 compared to that in conventional ZnSe(Te) scintillator, what is an indication of stronger nonradiative recombination in ZnSe doped with oxygen and aluminum [66].

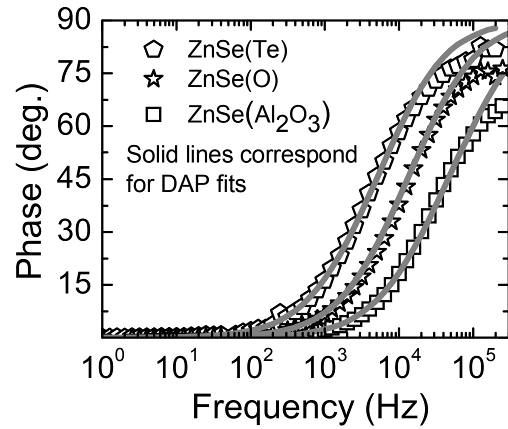

Fig. 4.2.3.3. Frequency dependence of phase shift between modulated excitation and luminescence response in ZnSe(Te) (pentagon), ZnSe(O) (stars), ZnSe(O,Al) (squares) at $h\nu_{exc}$ =2.58 eV.

4.4. Analysis of structure of the complex defects involving isoelectronic impurities

The higher rate of radiative recombination in the crystals containing oxygen impurity might be explained by different structure of tellurium- and oxygen-related complex defects, caused by different chemical properties of isoelectronic Te_{Se} and O_{Se}. The substitution of Se by Te_{Se} incurs local lattice strain and results in redistribution of the effective charge due to different covalent radii, 1.28 Å and 1.07 Å [67], and electronegativity, 2.16 and 2.43 on the Allen scale [68,69] for Te and Se, respectively. Thus, Te_{Se} repulses the closest zinc atom Zn_i and attracts zinc vacancy V_{Zn} and forms a complex defect $\{Te_{Se} + V_{Zn} + Zn_i\}$ serving as a deep acceptor, responsible for LE band in ZnSe [13,70,71]. The defect formation mechanism in oxygen-doped ZnSe is similar to that in ZnSe(Te) [29,72]. However, oxygen ions have smaller covalent radii, 0.57 Å, and higher electronegativity, 3.61, than that of Se. Therefore, substitute O_{Se} attracts Zn_i and repulses V_{Zn}. As a result, a complex defect $\{O_{Se} + V_{Zn} + Zn_i\}$ having different Zn_i and V_{Zn} configuration is formed. The different chemical properties of Te_{Se} and O_{Se} result in a different effective charge state of these associates, which affects the capture of free holes. The effective charge of substitutes Te_{Se} and O_{Se} can be evaluated from the electronegativities by estimating the chemical bond ionicity [73]. For this purpose the effective charges e^*_{ZnSe} e^*_{ZnTe} and e^*_{ZnO} of the corresponding bonds in the crystals with sp^3 bonding (in the unit of electron charge e) have been calculated as [73]

$$e^* = n \cdot \lambda . \qquad \textbf{(4.4.1)}$$

Here, n is the valency of the isoelectronic impurity, $\lambda = 1 - \exp[-0.5 \cdot (x_{(Se,Te,O)} - x_{Zn})^2]$ is ionicity of the corresponding bond, and x_{Se}, x_{Te}, x_O, x_{Zn} are the electronegativities of the corresponding atoms: x_{Se} =2.43, x_{Te} =2.16, x_O =3.61, x_{Zn} =1.59, yield e^*_{ZnTe} = 0.30, e^*_{ZnSe} = 0.59, and e^*_{ZnO} = 1.74. Finally, the effective charges of the substitutes Te_{Se} and O_{Se} at the low impurity density can be evaluated as the difference of the corresponding effective charges of the bonds: $\beta^*_{Te} = e^*_{ZnSe} - e^*_{ZnTe}$ = 0.29 and $\beta^*_O = e^*_{ZnSe} - e^*_{ZnO}$ = -1.15. The effective charges of Te_{Se} and O_{Se} have opposite signs.

To reveal the charge state of zinc vacancy, we measured EPR at liquid nitrogen temperature in the X-band frequency range. No EPR signal was detected. This is an indication that the zinc vacancy has paired electrons in its ground state. The highest possible value of the charge state of the interstitial Zn_i is +2. Thus, the total effective charge state of the associate $\{O_{Se}^{-1.15}+V_{Zn}^{--}+Zn_i\}$ is negative, in contrast to that of $\{Te_{Se}^{0.29}+V_{Zn}^{--}+Zn_i\}$. The high negative effective charge of the O_{Se}-related complex defect results in a large capture cross-section for holes compared to that of positively charged Te_{Se}-related complex defect. In II–VI semiconductors, the optical transition involving donor and acceptor pair proceeds in three steps [74]: i) capture of a free hole by acceptor level, ii) capture of a free electron by donor level, and iii) recombination of the bound electron and hole. Thus, the larger capture cross-section of the O_{Se}-related complex defect results in faster luminescence decay of the LE band.

It should be noted, that doping with Te is favorable for generation of V_{Zn} in close vicinity of Te_{Se}, whereas doping with O_{Se} generates interstitial Zn_i. Consequently, doping of ZnSe with both Te and O may compensate formation of the complex defects responsible for efficient light emission. Moreover, the effective charge of O_{Se} is by a factor of 4 higher than that of Te_{Se}, thus, even a small amount of oxygen in ZnSe(Te) might disturb the Te_{Se}-related defect formation and reduce the PL efficiency. This effect might occur also by unintentional doping of ZnSe(Te) with oxygen via the introduction of RE oxides into the melt to grow ZnSe codoped with RE ions.

Chater 5. *In situ* study of of variations of proton induced luminescence in ZnSe(Te) crystals

5.1. *In situ* study of of variation of luminescence spectra and carrier transients in the conventional ZnSe(Te) scintillation crystals

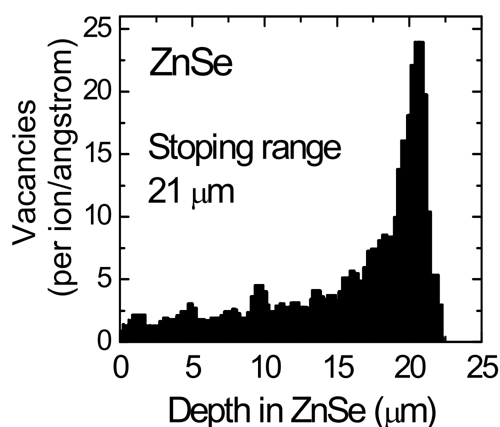

Fig. 5.1.1. TRIM simulated the defect distribution profile due to penetration of 1.6 MeV protons in ZnSe sample

The profile of the density of proton-beam-generated radiation defects has been simulated by TRIM [75]. The depth at which the large density of radiation defects is generated by 1.6 MeV protons (hereafter referred to as the stopping range) in ZnSe single crystal is 21 μm (Fig. 5.1.1). A sharp increase of the density of radiation defect occurs at the stopping range.

The study of photoconductivity (MW-PC) and luminescence responses after exposure of the sample to the 1.6 MeV proton beam have been carried out.

The photoconductivity profile was scanned by the MW-PC probes. The largest photoconductivity signal has been detected near the irradiated surface (Fig 5.1.2 (a).). In this region, the radiation defects density is low and nearly homogeneous. Thereby, in this region the MW-PC signal is mainly determined by the excess carriers. The carrier lifetime τ_{eff} estimated from the initial fast decay in the MW-PC transients is lower in the

range from 0 to 15 μm and correlates with the simulated stopping range of 1.6 MeV protons.

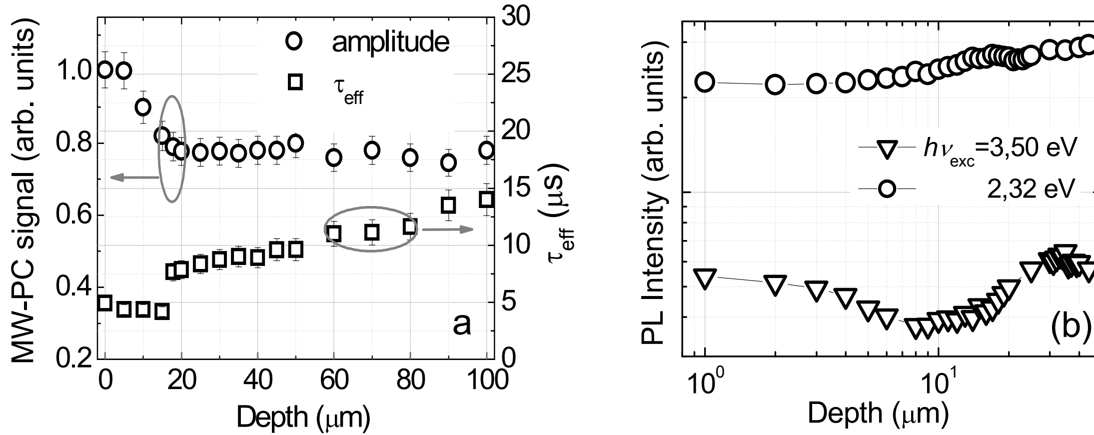

Fig. 5.1.2. The profiles of the effective carrier lifetime and the MW-PC signal obtained under pulsed laser excitation at $h\nu_{exc}$=3,50 eV (a) and the defect-related luminescence intensity as a function of the distance between the front surface and the excitation laser spot position on the side wall of the sample for bulk excitation at $h\nu_{exc}$=3.50 eV and for strongly absorbed ($h\nu_{exc}$=3.50 eV) excitation (b).

It might be assumed, that the layer of surface recombination of nonequilibrium carrier is of ~20 μm in thickness and is limited by the boundary of increased density of radiation defects.

The profiles of the defect-related photoluminescence intensity in the proton-irradiated ZnSe(Te) under surface ($h\nu_{exc}$=3.50 eV) and bulk ($h\nu_{exc}$=2.33 eV) excitation are shown in Fig. 5.1.2 (b). It is seen that at the surface excitation condition the luminescence efficiency decreases within the proton penetration layer. While at the bulk excitation condition luminescence efficiency gradually increases by increasing the scanning depth. Thus, it might be assumes that the *in situ* variation of the luminescence intensity (its reduction with the proton fluence) during irradiation is correctly reproduced by the luminescence light collected from the front surface. The profiling experiments were performed just after irradiation and after storage of the sample at room temperature for a few weeks.

The time-integrated luminescence spectra of non-irradiated ZnSe sample excited by laser pulse (LS-L) and by proton beam at a very small fluence (PI-L) are compared in Fig. 5.1.3 (a). The LS-L spectrum is multiplied by a factor of 40 to match the intensities of the defect-related luminescence band. The peak intensities of two luminescence bands as a function of fluence of 1.6 MeV protons *in situ* irradiation are presented in Fig. 5.1.3 (b). The fast decrease of luminescence intensities with increasing proton fluence is apparently caused by an increase of density of nonradiative recombination defects and destruction of centers of radiative recombination.

The MW-PC transients recorded at the different fluences accumulated during CW irradiation by 1.6 MeV protons are illustrated in Fig. 5.1.4 (a). The fast and slow decay components were observed. The effective decay time τ of the slow component as a function of the fluence is shown in Fig. 5.1.4 (b). A decrease of the effective decay time from 600 to 350 μs is evident for fluences in the range from 2×10^{12} to 2×10^{14} cm^{-2} and correlates with the luminescence intensity dependence in Fig. 5.1.3 (b).

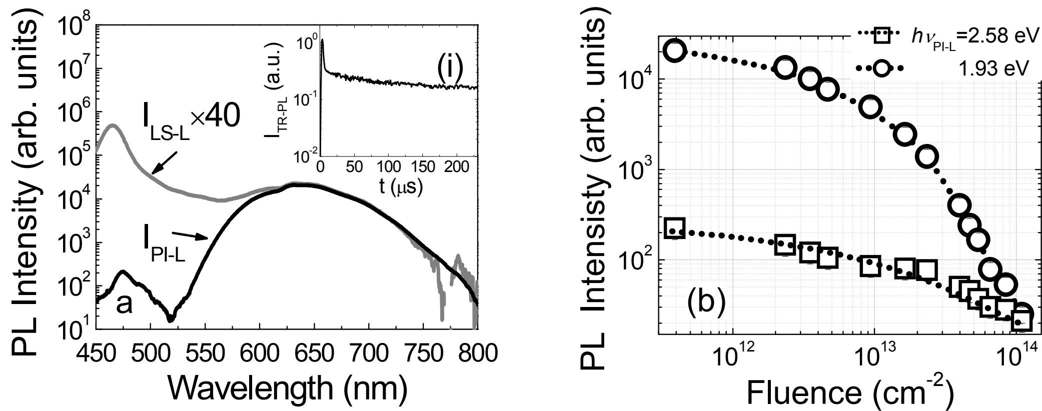

Fig. 5.1.3. The time-integrated luminescence spectra of non-irradiated ZnSe sample (black curve) and the sample under excitation by proton beam at small fluence (grey curve; magnification factor indicated) and decay transient for defect-related PL in the inset (a), and the peak intensities of two luminescence bands (peak wavelengths indicated) as a function of 1.6 MeV proton irradiation fluence (b).

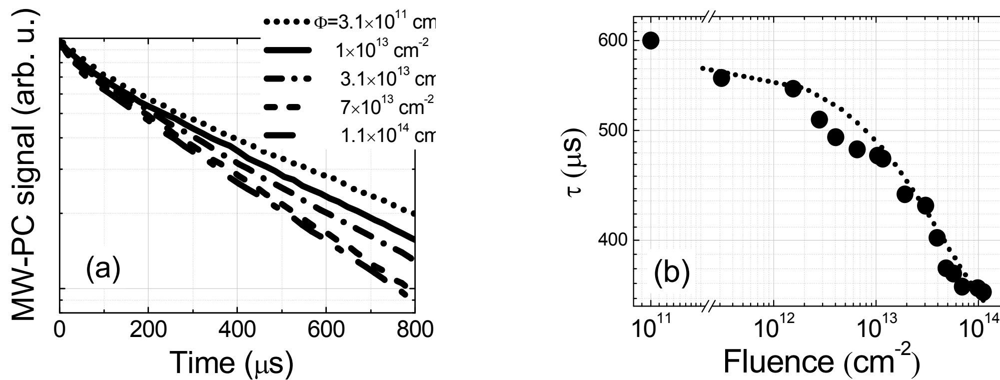

Fig. 5.1.4. MW-PC transients recorded after the fluence indicated is accumulated during the steady irradiation by 1.6 MeV protons (a) and the effective carrier lifetime as a function of 1.6 MeV proton irradiation fluence (b).

5.2. Peculiarities of the carrier pair generation and recombination mechanisms inherent to light and proton beam excitation

The evaluation of variation of parameters for nonradiative and radiative recombination during irradiation by high energy protons was performed. The proton-excited luminescence measured *in situ* during irradiation has been collected from the depth of up to ~20 μm.

The intensity and spectra of the luminescence induced by laser excitation and proton flux have been compared to evaluate the excess carrier density generated by protons and to relate it to the intensity of red luminescence induced by protons. To evaluate the average excess carrier density generated by the proton beam, the two spectra presented in Fig. 5.1.3 (a) were normalized to match intensities of the defect-related luminescence bands.

The inhomogeneity of the laser excitation and differences of luminescence signal integration in time were taken into account to enhance the precision in the evaluation of the density of excess carriers. The average density of the photogenerated excess carrier

has been evaluated by using the relation written by taking into account the carrier recombination and diffusion within the stopping range [76]:

$$\langle n\rangle = \frac{\tau_{R-L}^{in} E_L}{t_D A_L h\nu_{exc} d}[1-\exp(-\beta d)] = 2.9\times10^{14}\ \text{cm}^{-3}. \qquad (5.2.1)$$

Here, $E_L = 0.11$ μJ is the energy per laser pulse used in calibration measurements, $A_L = 3.1\times10^{-2}$ cm^2 is the laser beam spot area, $h\nu_{exc} = 3.5$ eV, $t_D \cong d^2/D = 2.7$ μs is the carrier diffusion time, where $D \cong 1.6$ cm^2/s is the ambipolar diffusion coefficient in ZnSe [77], $d = 20$ μm is the surface recombination depth, and $\tau_{R-L}^{in} \cong 3$ ns is the free carrier lifetime (see inset in Fig 5.1.3 (a)). Finally, the proton-induced carrier density n_p is evaluated to be $n_p = 40\langle n\rangle = 1.3\times10^{16}$ cm^{-3}. Here the factor 40 is the normalization constant evaluated from the spectra in Fig.5.1.3 (a).

The nonequilibrium carrier generation efficiency can be estimated as $k_P = n_p / N_P = 8\times10^6$ cm^{-3}, where $N_P = i_P\tau_{L-av}/e = 1.56\times10^9$ is the number of protons crossing the sample surface $A_P = 2$ cm^2, $i_P = 25$ nA is the beam current, $e = 1.6\times10^{-19}$ C, $\tau_{L\text{-}av} = 10$ ms (the luminescence signal integration time in proton- and laser- excited luminescence experiments was equal). The carrier generation efficiency (carrier pairs per micrometer) of the effective layer of $d \approx 20$ μm in depth is equal $\kappa_P A_{pr} = 25$ μm^{-1}pair^{-1}, where $A_{pr} = 3\times10^{-2}$ cm^2 is the total input area of a multifiber probe, is close to the values obtained for other wide-band-gap materials [78].

The defect introduction rate can be evaluated using the luminescence intensity reduction as a function of fluence. The excess carrier density decreases due to shortening of the carrier lifetime τ_{rd} caused by the radiation-induced centers of nonradiative recombination. The density of the radiation-induced defects is related to τ_{rd} by the relation

$$N_{rd} = \frac{1}{\sigma_{rd}\tau_{rd}v_T}. \qquad (5.2.2)$$

Here σ_{rd} and v_T is capture cross-section and thermal velocity, respectively. By using the carrier decay time $\tau_{R-L}^{as} \approx 210$ ns for the slow decay component estimated from PL decay kinetics measured in the non-irradiated ZnSe(Te) sample (see inset in Fig. 5.1.3(a)) and taking the typical values of σ_{rd}~10^{-14} cm^2 and v_T~10^7 cm/s, the defect density N_{rd0} is found to be 4.8×10^{13} cm^{-3}. The defect introduction rate $K_{P\text{-}R}$ can be estimated as

$$K_{P-R} = \frac{\Delta N_{rd}}{\Delta\Phi} \sim \frac{\Delta I_{P-L}}{\Delta\Phi}. \qquad (5.2.3)$$

Here $\Delta I_{P\text{-}L}$ is the change in proton-induced luminescence intensity caused by the change of proton fluence $\Delta\Phi$. Using the data presented in Fig 5.1.3 (c) for the proton-induced red luminescence, the value $K_{P\text{-}R} \cong 2$ cm^{-1} has been obtained.

Note, that the dominating carrier recombination mechanism is determined by the properties of excitation emission (see Fig. 5.1.3 (a)). The dominating recombination mechanism at photoexcitation is band-to-band (near-band-edge) optical transitions (see Fig. 5.1.3 (a)). Meanwhile, under the proton irradiation the major part of the carriers recombine through technologically-introduced deep level, while the band-to-band luminescence is by three orders of magnitude weaker. This difference might be imposed by different momentum conservation conditions in the photon-electron and proton-atom-electron interactions. In the former case, the momentum conservation is easily satisfied

due to the small momentum of photons. However, the generation of carriers by a proton having a large momentum is much more complicated. The conservation of momentum requires excitation of lattice vibrations and multi-particle (proton-electron-phonon) interactions to generate the carrier pair. There are many combinations in conservation of energy and momentum; those can be involved into these interactions. For high energy protons, a significant fraction of the absorbed energy goes into the excitations that carry momentum, and the average energy deposition E_i required to produce a carrier pair is estimated by the expression [79] $E_i \approx 2.8E_g + 0.6$ eV, which is valid for most semiconductors. The proton generated electrons and holes acquire quite different quasi-momenta, and direct radiative recombination is less probable in this case. Thus, the optical transition involving DAPs might be more efficient than the direct band-to-band transition. The similar redistribution between the DAP and band-to-band luminescence bands has been obtained in GaN [80] and polycrystalline CdS [81].

List of publications related to the thesis

Papers:

S1. **D. Shevchenko**, V. Gavryushin, J. Mickevičius, N. Starzhinskiy, I. Zenya, A. Zhukov, G. Tamulaitis, Emission properties of ZnSe scintillation crystals co-doped by oxygen and aluminum, J. Lumin. **143** (2013) 473.

S2. **D. Shevchenko**, J. Mickevičius, N. Starzhinskiy, I. Zenya, A. Zhukov, G. Tamulaitis, Luminescence in ZnSe scintillation crystals co-doped with oxygen and aluminum, Nucl. Instr. Meth. Phys. Research A **2014** (2013) 14.

S3. E. Gaubas, T. Ceponis, A. Jasiunas, J. Pavlov, A. Tekorius, **D. Shevchenko**, K. Katrunov, V. Kovalevskij, V. Remeikis, S. Galkin and G. Tamulaitis, In situ variations of proton induced luminescence in ZnSe crystals, J. Phys. D **47** (2014) 265102.

Conference contribution:

K1. **D. Shevchenko**, J. Mickevičius, G. Tamulaitis, N. Starzhinskiy, K. Katrunov, V. Ryzhikov, Photoluminescence Study of ZnSe Scintillating Crystals Doped with Isovalent Tellurium and Oxygen, Abstract of the 40th "Jaszowiec 2011" International Conference on the Physics of Semiconducting Compounds , Krynica- Zdroj, Poland, June 25- July 01, 2011.

K2. **D. Ševčenko**, J. Mickevičius, G. Tamulaitis, N. Starzhinskiy, K. Katrunov, V. Ryzhikov, Izovalentinemis telūro bei deguonies priemaišomis legiruotų ZnSe scintiliacinių kristalų priemaišinė fotoliuminescencija, 39-oji Lietuvos nacionalinė fizikos konferencija, Vilnius, Lietuva, spalio 6- 8 d., 2011.

K3. **J. Mickevičius**, D. Ševčenko, G. Tamulaitis, N. Starzhinskiy, K. Katrunov, V. Ryzhikov, Photoluminescence of isovalently dopedZnSe crystals, 11th International

Conference on Inorganic Scintillators and Their Application, Giessen, Germany, September 11-16, 2011.

K4. **D. Shevchenko**, J. Mickevičius, G. Tamulaitis, N. Starzhinskiy, K. Katrunov, V. Ryzhikov, Influence OF Aluminum co-doping on Emission Properties of ZnSe Scintillation Crystals, International conference of students and young researchers in theoretical and experimental physics HEUREKA-2012, Lviv, Ukraine, April 19-22 2012.

K5. **D. Shevchenko**, J. Mickevičius, G. Tamulaitis, N. Starzhinskiy, K. Katrunov, Study of photoemission properties in ZnSe scintillation crystals co-doped by aluminium, 14th International Conference-School "Advanced Materials and Technologies", Palanga, Lithuania, August 27-31, 2012.

K6. **D. Ševčenko**, P. Cicėnas, T. Čeponis, E. Gaubas, A. Jasiūnas, V. Kalendra, J. Mickevičius, G. Tamulaitis, N. Starzhinskiy, I. Zenya, A. Zhukov, 40-oji Lietuvos nacionalinė fizikos konferencija, Vilnius, Lietuva, birželio 10- 12 d., 2013 m.

K7. **D. Shevchenko**, J. Mickevičius, N. Starzhinskiy, I. Zenya, A. Zhukov, G. Tamulaitis, Study of photoluminescence kinetics in ZnSe scintillation crystals, 15th International Conference-School "Advanced Materials and Technologies", Palanga, Lithuania, August 27-31, 2013.

K8. **D. Shevchenko**, J. Mickevičius, N. Starzhinskiy, I. Zenya, A. Zhukov, G. Tamulaitis, Kinetics of defect-related photoluminescence in ZnSe scintillation crystals, Advanced scintillation materials 2013, Kharkov, Ukraine, Septemper 23-27, 2013 m.

K9. **D. Shevchenko**, J. Mickevičius, N. Starzhinskiy, I. Zenya, A. Zhukov, G. Tamulaitis, Study of defect-related luminescence in ZnSe scintillation crystals co-doped with oxygen and aluminum, International Workshop on Radiation Imaging Detectors iWoRID 2014, Trieste, Italy, June 23-27, 2014.

Information about the author

Name and surname	Dmitrij Ševčenko (Dmitriy Shevchenko)	
Birth date and place:	April 7, 1985, Vilnius, Lithuania	
E-mail:	sevcenkoff@gmail.com	
Education:	2004	Secondary education, Vilnius "Sofijos Kovalevskajos" secondary school
	2008	Bachelor degree in physics, Vilnius University
	2010	Master degree in physics, Vilnius University
	2010-2014	Doctoral studies at Vilnius University
Scientific experience:	2007-2008	Laboratory assistant at Department of Semiconducting Physics, Vilnius University
	2008-2009	Technician at the Institute of Applied Research, Vilnius University
	2009-2013	Engineer at the Institute of Applied Research, Vilnius University
	2013-2015	Junior scientific researcher at the Institute of Applied Research, Vilnius University

Specialization:

Optical characterization of semiconductors by using optical spectroscopy techniques:

- photoluminescence spectroscopy,
- time-resolved photoluminescence spectroscopy,
- luminescence life time measurements in frequency domain,
- measurements of absolute quantum yield
- photoluminescence excitation spectroscopy

Publications:

4 research papers in journals listed in Thomson Reuter ISI WOS^{SM}, 9 conference theses

References

[1] J.R. Lakowicz, *Principles of Fluorescence Spectroscopy*, Kluwer Academic/Plenum, New York, 1999.
[2] J.C. de Mello, H.F. Wittmann, and R.H. Friend, Adv. Mater. **9** 230 (1997).
[3] http://www.fi.lt/BARTL/index.html.
[4] A. Tekorius, E. Gaubas, T. Ceponis, A. Jasiunas, A. Uleckas , J. Vaitkus, and Velicka, 2012 Proc. 4th Int. Conf. on Radiation Interaction with Material and Its Use in Technologies (Kaunas) pp 282–5.
[5] E. Gaubas *et al*, Nucl. Instrum. Meth. Phys. Res. B **307** (2013) 370.
[6] E. Gaubas, A. Uleckas, J. Vaitkus, P. Raisanen, and P. Tikkanen, Review Sci. Instrum. **81** (2010) 053303.
[7] E. Gaubas, T. Ceponis, A. Jasiunas, J. Pavlov, A. Tekorius, D. Shevchenko, K. Katrunov, V. Kovalevskij, V. Remeikis, S. Galkin and G. Tamulaitis, J. Phys. D **47** (2014) 265102.
[8] E.V. Gusev and K.K. Turoverov, J. Appl. Spectrosc. **29** (1978) 844 (translated from Zhurnal Prikladnoi Spektroskopii **29** (1978) 844).
[9] K. M. Lee, Le Si Dang and G. D. Watkins Solid State Commun. **35** (1980) 527.
[10] D.J. Dunstan, J.E. Nicholls, B.C. Cavenett and J.J. Davies, J. Phys. C Solid State **13** (1980) 6409.
[11] M. Godliewski, W. E. Lamb and B. C. Cavenett, J. Lumin. **24**/**25** (1981)173.
[12] D. Verety, J.J. Davies, J.E. Nicholls, and F. J. Bryant, J. Appl. Phys. **52** (1981) 737.
[13] R. Baltramiejunas, V. D. Ryzhikov, V. Gavryushin, A. Kazlauskas, G. Raciukaitis, V.I. Silin, D. Juodzbalis, and V. Stepankevicius, J. Lumin. **52** (1992) 71.
[14] V. Ryzhikov, G. Tamulaitis, N. Starzhinskiy, L. Gal'nichenskii, A. Novickovas and K. Kazlauskas, J. Lumin. **101** (2003) 45.
[15]. G.F. Neumark, Mat. Sci. Eng. **R21** (1997) 1.
[16] M. Prokesch, K. Irmescher, J. Gebauer and R. Krause-Rehber, J. Crystal Growth **214**/**215** (2000) 988.
[17] D.C. Oh, T. Takai, T. Hanada, M.W. Cho and T. Yao *et al.*, J. Appl. Phys. 96 (2004) 7332.
[18] R.K.Watts, J. Matt. Sci. **8** (1973) 1201.
[19] J.S. Ko and W. G. Spitzer, J. Appl. Phys. **53** (1982) 3894.
[20] K. Irmscher, M. Prokesch, Mat. Sci. Eng. **B80** (2001) 168.
[21] U. V. Desnica, Prog. Crystal Growth and Charact. **36** (1998) 291.
[22] M.Aven and N. Woodbury, J. Appl. Phys. Lett. **1** (1962) 53.
[23] V. Ryzhikov, N. Starszynskiy, K. Katrunov, L Gal'chinetskii, I Rybalka, Funct. Mater. **9** (2002) 143.
[24] Yu.F.Vaksman, N.V.Malushin , V.M. Skobeeva, S.Agilera Morales, and V.V. Serdyuk, J. Appl. Spectrosc. **21** (1974) 1105.
[25] J.Aranovich, A.l. Fahrenbruch, and R.H. Bube, J. Appl. Phys. **49**(1978) 2584.
[26] В.С. Вавилов, А.А. Клюканов, К.Д. Сушкевич, М.В. Чукиев, Р.Р. Чукичев, Р.Р. Резванов, Е.К. Сушкевич, ФТТ **39** (1997) 1526.
[27] P.P Debye and E.M. Conwell, Phys. Rev. **93** (1954) 693.
[28] E.F. Schubert, *Doping in III-V Semiconductors*, Cambridge University Press, Cambridge, 1993, p. 36.
[29] V.D. Ryzhikov, N.G. Starzhinskiy, L.P. Gal'chinetskii, V.I. Silin, G. Tamulaitis, E.K. Lisetskaya, Int. J. Inorg. Mater. **3** (2001) 1227.
[30] N.K. Morozova et, L.D. Nazarova, I.A. Karetnikov, V.G. Galastyan, L.P. Gal'chinetskii, V.D. Ryzhikov, Sov. Phys. Semicond. **29** (1995) 1678.

[31] В.В.Осипов, М.Г.Фойгель, Физика и техника полупроводников **10** (1976) 522.
[32] V.P. Makhniy, S.V. Khusnutdinov, and R.Jakel, Inorg. Mater. **47** (2011) 746.
[33] N.G. Starzhinskiy, V.D. Ryzhikov, L.P. Gal'chinetskiy, L.L. Nagornaya, V.I. Silin, Voprosy Atomnoy Nauki i Tekhniki, Ser.: Radiation Damage Physics and Radiation Technology, **88** No.5 (2005) 58 (in russian).
[34] G. Jones and J. Woods, J. Lumin. **9** (1974) 389.
[35] H.G. Grimmeis, C. Ovren, W. Ludwig and R. March, J. Appl. Phys. **48** (1977) 5122
[36] S. Wang and X.W. Fan, J. Lumin. **40- 41** (1988) 802.
[37] Даниэль Кюри, *Люминесценция кристаллов*, Издательство иностранной литературы, Москва, 1961, стр. 61.
[38] N.D. Nedeoglo, A.N. Avdonin, G.N. Ivanova, D.D. Nedeoglo, G.V. Kolibaba, V.P. Sirkeli, J. Lumin. **112** (2005) 62.
[39] S. Kishida, K. Matsuura, H. Nagase, and I. Tsurumi, Phys. Stat. Sol. (a) **103** (1987) 613
[40] Ю.Н. Дмитриев, В.Д. Рыжиков, Л.П. Гальчинецкий, *Темодинамика изовалентного легирования кристаллов полупроводниковых соединений типа* AIIBVI, ВНИИ Монокристаллов, Харьков, 1990, стр. 21.
[41] E. Kuokštis, G. Tamulaitis, *Plačiatarpių puslaidininkių technologija ir prietaisai*, Vilniaus universitetas, Vilnius, 2008, p. 23.
[42] N.G. Starzhinsky, I.M. Zenya, K.A. Katrunov, V.D. Rizhikov, Tehnologija i konstruirovanie v jelektronnoj apparature **3** (2009) 51 [in russian].
[43] М.П.Кулаков, А.В. Фадеев, Изв. АН СССР Неорг. материалы **19** (1988) 347.
[44] M. Ichimura, Solid-State Electron. **50** (2006)1761.
[45] R.A. Brown and M.L. Burns, Phys. Lett. **32** (1970) 513.
[46] H.G. Grimmeis, C. Ovren, and R. March , J. Appl. Phys. **50** (1979) 6331.
[47] S.W.S. McKEEVER, *Thermoluminescence of solids*, Cambridge, London, New York, Rochelle, Melbourne, Sydney, 1988, pp.28-29.
[48] D.G. Thomas, J.J. Hopfield, and W.M. Augustyniak, Phys. Rev. **140** (1965) 202.
[49] F. Williams, J. Lumin. **7** (1973) 35.
[50] F.E. Williams, J. Phys. Chem. Solids **12** (1960) 265.
[51] A. Debernardi, M. Cardona, Phys Rev. B **54** (1996) 11305.
[52] B. Segall, D. T. F. Marple, *in Physics and Chemistry of II-VI compounds*. M. Aven, J. S. Prener (eds.), North-Holland Publishing Company, Amsterdam, 1967, p. 335.
[53] G. Lucovskiy, Solid State Commun. **88** (1993) 879.
[54] V.Gavryushin, Lithuanian J. Phys. **42** (2002) 219.
[55] V.Gavryushin, JETP Letters **78** (2003) 309
[56] A.Kopylov and A.Pihtin, Sov. Phys.Solid State, **16** (1975) 1837; Sov.Phys.Tech. Semicond., **10** (1976) 15.
[57] K.A. Katrunov, N.G. Starzhynskiy, Yu.V. Malyukin, V.I. Silin, I.M. Zenya, G. Tamulaitis, Nucl. Instr. and Meth. A **622** (2010) 139.
[58] Y. Nabetani, T. Mukawa, T. Okuno, Y. Ito, T. Kato, T. Matsumoto, Matter. Sci. Semicond. Process. **6** (2003) 343.
[59] W. Shan, W. Walukiewicz, J.W. Ager III, K.M. Yu, E.E. Haller, Y. Nabetani, T. Mukawa, Y. Ito, and T. Matsumoto, Appl. Phys. Lett. **83** (2003) 299.
[60]. K. Akimot, H. Okuyama, M. Ikeda, and Y. Mori, Appl. Phys. Lett. **60** (1992) 91.
[61] D.J. Chadi, J. Cryst. Growth. **138** (1994) 295.
[62] J.-H. Lee. J. Wu, and J.C. Grossman, Phys. Rev. Lett. **104**, 016602 (2010).
[63] S. Adachi and T.Taguchi, Phys. Rev. B **43** (1991) 9569.
[64] M.A. Arvizu, S.A. Tomas, M. Morales-Luna, J. Santoyo-Salazar, J.O. García-Torija, O. Zelaya-Angel, Int. J. Thermophys **33** (2012) 2035.

[65] J. Ni, Z. Wu, X. Lin, J. Zheng, S. Li, J. Li, and J. Kang, J. Mater. Research **27** (2012) 730.
[66] D. Shevchenko, J. Mickevičius, N. Starzhinskiy, I. Zenya, A. Zhukov, G. Tamulaitis, Nucl. Instr. and Meth. A **749** (2014) 14.
[67] P. Pyykkö, M. Atsumi, Chem. Eur. J. **15** (2009) 12770.
[68] L.C. Allen, J. Am. Chem. Soc. **111** (1989) 9003.
[69] J.E. Huheey, E.A. Keiter, and R.L. Keiter, Inorganic Chemistry: Principles of Structure and Reactivity, fourth ed., HarperCollins, New York, 1993.
[70] V. Ryzhikov, B. Grinyov, S. Galkin, N. Starzhinskiy, I. Rybalka, J. Cryst. Growth **364** (2013) 111.
[71] O.V. Vakulenko, V.N. Kravchenko, V.D. Ryzikov, V.I. Silin, and N.G. Starzhynskii Semiconductors **31** (1997) 1041 (translated from Fizika i Tekhnika Poluprovodnikov. **31** (1997) 1211).
[72] N.K. Morozova et, I.A. Karetnikov, V.V. Blinov, E.M. Gavrishchuk ., Semiconductors **35** (2001) 24 (translated from Sov. Phys. Semicond. **35** (2001) 25).
[73] E.E. Ovechkina, V.M. Koshkin L.A. Sysoev, J. Struct. Chem. **10** (1969) 150 (translated from Zhurnal Strukturnoi Khimii **10** (1969) 156).
[74] J. Krustok H. Collan, and K. Hjelt, J. Appl. Phys. **81** (1997) 1443.
[75] The software can be downloaded for free http://www.srim.org.
[76] E. Gaubas, T. Ceponis, A. Jasiunas, J. Pavlov, A. Tekorius, D. Shevchenko, K. Katrunov, V. Kovalevskij, V. Remeikis, S. Galkin and G. Tamulaitis, J. Phys. D **47** (2014) 265102.
[77] V. Netiksis,S. Juodkazis, M. Petrauskas, B. Honerlage, R. Levy, and Y. Ding, Optics Commun. **126** (1996) 247.
[78] M. Moll, Nucl. Instrum. Meth. Phys. Res. A **565** (2006) 202
[79] H. Spieler, *Semiconductor detector systems* (Oxford University Press, New York, 2005)
[80] E Gaubas, T. Ceponis, A. Jasiunas,V. Kovalevskij, D. Meskauskaite, J. Pavlov, V. Remeikis, A. Tekorius, and J. Vaitkus, Appl. Phys. Lett. **104** (2014) 062104.
[81] E. Gaubas, I. Brytavskyi, T. Ceponis, A. Jasiunas, V. Kalesinskas, V. Kovalevskij, D. Meskauskaite, J. Pavlov, V. Remeikis, G. Tamulaitis, and A. Tekorius, J. Appl. Phys. **115** 243507 (2014).